Master Thesis of the University of Ulsan

Subject: Tailoring high-performance ceramic electrolyte nanostructures by sputtering and its application in thin-film solid oxide fuel cells

Department of Mechanical and Automotive Engineering

University of Ulsan

Ulsan, Korea

Yue Teng

2022

Subject: Tailoring high-performance ceramic electrolyte nanostructures by sputtering and its application in thin-film solid oxide fuel cells

Supervisor: Prof. Yoon Ho Lee

Author: Yue Teng

Department of Mechanical and Automotive Engineering
University of Ulsan

A dissertation submitted to the faculty of the University of Ulsan in partial fulfillment the requirement for the degree of Master of Philosophy in the Department of Mechanical and Automotive Engineering.

Ulsan, Korea

August, 2022

Approved by

Professor Yoon Ho Lee

To Approve the Submitted Dissertation for the Degree of

Master of Science in Mechanical and Automotive Engineering

By

Yue Teng

Title: Tailoring high-performance ceramic electrolyte

nanostructures by sputtering and its application in thin-film solid

oxide fuel cells

August 2022
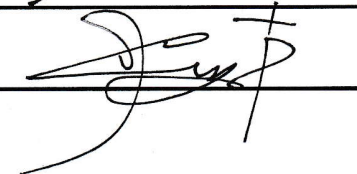
Committee Chair Professor Bo Hung Kim

Committee   Professor Dong Kim

Committee   Professor Yoon Ho Lee

Graduate School

University of Ulsan, South Korea

Yue Teng 의 공학석사학위 논문을 인준함

심사위원장　　김보흥　　(인)

심사위원　　　김동　　　(인)

심사위원　　　이윤호　　(인)

울산대학교 대학원

2022 년 8 월

ABSTRACT

Solid oxide fuel cell (SOFC) is a new type of green energy technology developed in recent years, which has the advantages of no corrosion, high energy conversion efficiency, strong fuel adaptability and long life. A solid oxide fuel cell is an all-solid-state fuel cell that uses a ceramic material (YSZ, GDC) that can conduct oxygen ions as an electrolyte. Since only two phases (gas phase and solid phase) are required, the principle is more efficient than any other fuel, so the principle is more straightforward than any other fuel cell. SOFC does not have the electrolyte management issues faced by phosphoric acid fuel cells (PAFC) and molten carbonate fuel cells (MCFC). The high operating temperature also means that no precious metal electrocatalyst is required, clean and efficient energy.

However, at the same time, the exceptionally high working temperature of SOFC has higher requirements on the thermal stability, high-temperature strength, electronic conductivity, thermal expansion matching and chemical stability of each component, which increases the difficulty of material selection. The anode or cathode supported electrolyte film can be prepared to reduce the fuel cell's internal resistance by reducing the electrolyte's thickness. This paper uses the magnetron sputtering technology in physical vapor deposition (PVD) to prepare thin-film electrolytes. It has many advantages, such as high deposition rate, wide sputtering range, high density of film formation, and sputter deposition of large-area targets.

With the continuous development and improvement of magnetron sputtering technology, the properties of thin films have been greatly improved. However, the process conditions during the sputtering

process play an essential role, and the sputtering conditions have become the main factor affecting the properties of the thin film/substrate. In this experiment, the effects of different sputtering conditions on the structure and properties of the electrolyte film were studied by changing the process conditions such as sputtering pressure, sputtering power, and the distance from the target to the substrate.

During the preparation of fuel cells, due to the difference in thermal expansion coefficient and elastic modulus of the matrix and film materials, each component's degree of shrinkage and expansion is different, and residual stress will be generated in the film. The excessive residual stress will reduce the strength of the material. Moreover, even lead to peeling and tearing of the film, failing the film structure. Therefore, it is of great significance to accurately measure the residual stress of the fuel cell film. In this paper, XRD is used to analyze the stress state of the film. The experiments show that with the increase of sputtering pressure, the stress state of the YSZ film changes from compressive stress to tensile stress, and the lattice spacing is calculated according to Bragg's law. As a result, the lattice spacing is more significant than In the normal phase, the existence of residual stress is proved.

To characterize the effect of electrolytes prepared under different sputtering pressure conditions, each electrolyte was applied on AAO-supported SOFCs composed of Ni anode and Pt cathode. No obvious defects or pinholes were seen in the electrolyte, while the electrodes exhibited a highly porous structure that provided sufficient channels for the reactants. The formed thin film solid oxide fuel cell was electrochemically characterized, and finally, the YSZ thin film solid oxide fuel cell prepared at 3mTorr sputtering pressure achieved an open-circuit voltage (OCV) of 1.043 V, and a maximum power density

of $1.593W/cm^2$ were achieved at 500 °C, providing guidance and reference for improving and improving the film properties.

Key words：Thin Film Solid Oxide Fuel Cell；Magnetron Sputtering；Sputtering Conditions ； Residual Stress ； Electrochemical Characterization；Yttria Stabilized Zirconia.；Anodic Aluminum Oxide.

ACKNOWLEGEMENTS

TABLE OF CONTENTS

LIST OF FIGURES

VIII

LIST OF TABLES

ABBREVIATIONS

AAO	Anodic Aluminum Oxide
AFC	Alkaline Fuel Cell
ALD	Atomic Layer Deposition
ALE	Atomic Layer Etching
APCVD	Atmospheric Pressure Chemical Vapor Deposition
CVD	Chemical Vapor Deposition
DC Sputtering	Direct Current Sputtering
EIS	Electrochemical Impedance Spectroscopy
GDC	Gadolinium Doped Ceria
IT-SOFC	Intermediate Temperature Solid Oxide Fuel Cell
LAMOX	$La_2Mo_2O_9$
LPCVD	Low Pressure Chemical Vapor Deposition
LSCM	$La_{0.7}Sr_{0.3}Cr_{0.5}Mn_{0.5}O_{3-\delta}$
LSGM	$La_{0.9}Sr_{0.1}Ga_{0.8}Mg_{0.2}O_{3-\delta}$
LSM	Lanthanum Strontium Manganite
LT-SOFC	Low Temperature Solid Oxide Fuel Cell
MCFC	Molten Carbonate Fuel Cell
MOCVD	Metal Organic Chemical Vapor Deposition
NiO	Nickel Oxide
OCV	Open Circuit Voltage
ORR	Oxidation Reduction Reaction

PAFC	Phosphoric Acid Fuel Cell
PEALD	Plasma Enhanced Atomic Layer Deposition
PECVD	Plasma Enhanced Chemical Vapor Deposition
PEMFC	Proton Exchange Membrane Fuel Cell
PVD	Physical Vapor Deposition
RF Sputtering	Radio Frequency Sputtering
SDC	Samarium Doped Ceria
SEM	Scanning Electron Microscopy
SNDC	$Sm_{0.075}Nd_{0.075}Ce_{0.85}O_{2-\delta}$
SOFC	Solid Oxide Fuel Cell
TFD	Thomas Fermi Dirac
TF-SOFC	Thin Film Solid Oxide Fuel Cell
TPB	Triple Phase Boundary
VTM	Vaccum Thin-film Materials
XRD	X-ray Diffraction
YSZ	Yttria Stabilized Zirconia

CHAPTER 1. Introduction

1.1 Fuel Cells Fundamentals

1.1.1 Introduction to Fuel Cells

A fuel cell is a new power generation battery different from traditional batteries. It is a power generation device that converts the Gibbs free energy part of the chemical energy of fuel into electrical energy through an electrochemical reaction, which is not limited by the Carnot cycle effect. So it has exceptionally high efficiency[1]. It is considered the fourth type of power generation technology after hydropower, thermal power, and nuclear power. In addition, fuel cells use fuel and oxygen as raw materials. There are no mechanical transmission parts in the middle process, so the generation of harmful gases is significantly reduced[2]. Thus, fuel cells promote energy utilization efficiency and protect the environment and are known as the most promising power generation technology today.

So far, fuel cells have more than 160 years of development history. As early as 1839, G-rove used platinum wire as the electrode, sulfuric acid as the electrolyte, hydrogen, and oxygen as the fuel, and successfully carried out the reverse reaction of the traditional water electrolysis, resulting in an electric current, creating the world's first model of a fuel cell[3]. In 1889, L.Mond and C.Langer used platinum as the electro-catalyst and the drilled platinum as the current collector to assemble a fuel cell. The battery's output voltage was 0.73V when the working current density was $3.5mA/cm^2$. This research is very close to modern fuel cells[4]. In the 1960s, fuel cells were first used as

auxiliary power sources on the Apollo lunar spacecraft of the National Aeronautics and Space Administration, which positively contributed to the human landing on the moon[5] , and fuel cell technology has developed rapidly.

1.1.2 The composition and working principle of fuel cell

A fuel cell is an energy conversion device. According to the electrochemical principle, the chemical energy stored in the fuel and oxidant is directly converted into electric energy, essentially a redox reaction. The main components of a fuel cell are electrodes, electrolyte separators, and current collectors.

The electrode is mainly divided into the cathode and the anode. The fuel cell electrode is usually a porous structure, which is different from the general fuel cell. The main reason for designing fuel cell electrodes into porous structures is that most fuels and oxidants used in fuel cells are gases (argon, oxygen, hydrogen). The solubility of a gas in the electrolyte is low. Therefore, to improve the current density of the fuel cell and increase the surface area of the electrode involved in the reaction, a porous structure electrode is designed[6].

The primary function of the electrolyte diaphragm is to separate the oxidant and reductant from each other and to conduct ions. The current collector, also known as bipolar plate, has the functions of collecting the current, separating oxidant and reducing agent, and guiding reactive gas.

During the operation of the fuel cell, the fuel gas and the oxidizing gas enter from the anode end and the cathode end of the fuel cell, respectively. The fuel gas emits electrons at the anode, which are conducted to the cathode to combine with the oxidizing gas to produce

ions. Due to the action of the electric field, the ions are transferred from the electrolyte to the anode, and the fuel gas forms a loop reaction and generates an electric current. Fuel cells generate heat during operation due to electrochemical reactions and internal resistance. The anode and cathode are porous structures, which are favorable for introducing reaction gas and the discharge of products. The electrolyte usually exhibits a dense structure, which blocks the internal short circuit of the fuel cell caused by the mixing of the two gases. The electrolyte also plays the role of transporting ions, separating fuel gas, an oxidizing gas.

1.1.3 Classification of fuel cells

Fuel cells can be classified according to different types of electrolyte into five categories, Alkaline fuel cell (AFC), Phosphate acid fuel cell (PAFC), Molten carbonate fuel cell (MCFC), Solid oxide fuel cell (SOFC), and Proton exchange membrane fuel cell (PEMFC) [7].

Alkaline fuel cell (AFC) technology is the earliest developed fuel cell technology, also known as the first generation of fuel cells, and still has specific development potential today [8]. Phosphoric acid fuel cell (PAFC) is currently the most mature technology. It has entered commercial applications and mass production, but it is currently mainly used in regional power stations due to high material costs[9]. As second-generation fuel cells, molten carbonate fuel cells (MCFCs) are mainly used in equipment power generation. However, today, the third-generation fuel cell, solid oxide fuel cell (SOFC), has outstanding features such as its all-solid-state structure, higher energy efficiency, and wide adaptability to various gases (gas, natural gas, mixed gas) [10]. As a result, it is now widely used and is also the focus of this paper. The fourth-generation fuel cell, Proton exchange membrane fuel

cell (PEMFC), has high energy efficiency and density, small volume and weight, short start time, and an extremely safe operation state. It is currently developing gradually, and there is much room for development in the future.

The most commercial fuel cell types are solid oxide fuel cells and proton exchange membrane fuel cells. These two fuel cells are described below.

A solid oxide fuel cell (SOFC) is a fully solid-state chemical power generation device that directly converts the chemical energy stored in fuels and oxidants into electric energy at medium and high temperatures[11]. Due to the all-solid structure, the structure of solid oxide fuel cells is diverse to meet different needs. The main fuel cell structures include tubular, flat-plate, sleeve-type, and single-block laminated structures. SOFCs of different structural types have advantages and disadvantages in structure, performance, and preparation.
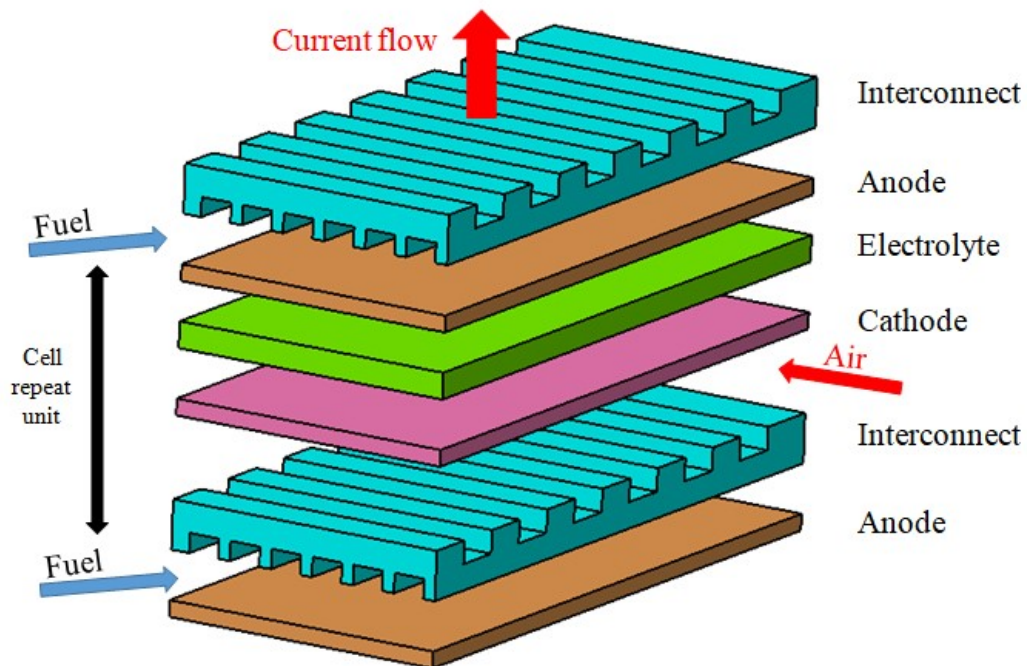
Figure 1. Schematic diagram of solid oxide fuel cells (SOFCs)

In this experiment, a flat-type solid oxide fuel cell is used, which consists of an anode, an electrolyte, and a cathode to form a single cell. The primary function of anode and cathode is to dredge electrons and provide diffusion channels for reactant gas and generated gas. The working principle of the solid oxide fuel cell is that the solid electrolyte separates the gases on both sides. Due to the difference in oxygen partial pressure on both sides of the cathode and the anode, a potential chemical gradient of oxygen is generated. The oxygen ions that have gained electrons move to the anode through the solid electrolyte, releasing electrons from the anode, forming a voltage at the two poles. The anode, cathode, and overall reaction equations that take place are:

$$\text{Anode：} \quad O^{2-} + H_2 \rightarrow H_2O + 2e^-$$

$$\text{Cathode:} \quad \frac{1}{2}O_2 + 2e^- \rightarrow O^{2-}$$

$$\text{Total reaction equation:} \quad H_2 + \frac{1}{2}O_2 \rightarrow H_2O$$
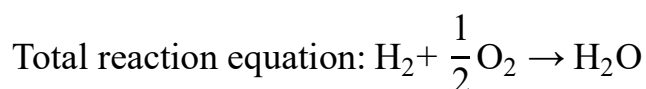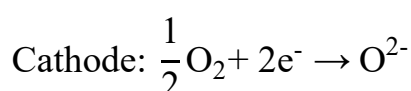
In principle, solid oxide fuel cells are ideal fuel cells. There is a high operating temperature (usually 800-1000°C), the chemical reaction rate of the cathode and anode is significant, and it is close to thermodynamic equilibrium[12] At the same time, it has many advantages, such as high current density and power density, wide fuel adaptability, high energy conversion rate, all-solid-state modular assembly, and zero pollution[13]. It is used as a fixed power station in civil fields such as large-scale centralized power supply, medium-sized power distribution, and small household heat and power cogeneration[14]. It also has broad application prospects as a power source for transmission, a power source for traffic vehicles, and a mobile power source. After the 1990s, under the premise of advancing

material science and process technology, countries worldwide have conducted in-depth research on the materials required for SOFC. They plan to realize commercialization as soon as possible.

A proton exchange membrane fuel cell (PEMFC), also known as solid polymer electrolyte fuel cell. It is essentially equivalent to the reverse process of water electrolysis. It consists of an anode, cathode, and proton exchange membrane. The hydrogen fuel is oxidized at the anode, the oxidant is reduced at the cathode, and the proton exchange membrane acts as the electrolyte. Since the proton exchange membrane can only conduct protons when the fuel cell is working, the hydrogen protons can directly pass through the proton exchange membrane to the cathode. At the same time, the electrons reach the cathode through the external circuit, generating direct current. The anode, cathode, and overall reaction equations that take place are:

$$\text{Anode: } H_2 \rightarrow 2H^+ + 2e^-$$

$$\text{Cathode: } \frac{1}{2}O_2 + 2H^+ + 2e^- \rightarrow H_2O$$

$$\text{Total reaction equation：} H_2 + \frac{1}{2}O_2 \rightarrow H_2O$$
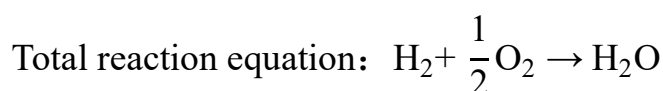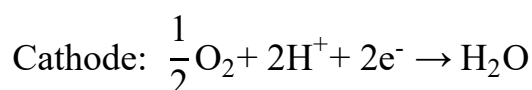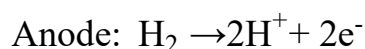
PEMFC has many advantages. The process of fuel cell power generation does not involve hydrogen and oxygen combustion, so it is not limited by the Carnot cycle and has high energy conversion efficiency. PEMFC has low operating temperature, fast fuel cell startup, relatively simple fuel cell structure, easy operation, lightweight, and is convenient for assembly and maintenance[15]–[18]. The performance of the proton exchange membrane has a significant influence on the performance of the fuel cell. The quality of the membrane directly affects the service life of the fuel cell. The reason is that the proton

exchange membrane provides a channel for the transfer and transportation of protons, and the protons pass through the exchange membrane from the anode to the cathode, forming a loop with the electron transfer of the external circuit to generate a current. Proton exchange membrane fuel cells are considered the energy source of choice for electric vehicles stationary power stations[19]. However, because the fuel cell is difficult to manufacture and the cost is exceptionally high, the temperature and water content requirements are incredibly high, and the technology is not yet fully mature, and further research is still required[20].

	AFC	PAFC	MCFC	SOFC	PEMFC
Electrolyte	Liquid KOH (Immobilized)	Liquid H_3PO_4 (Immobilized)	Molten Carbonate	Ceramic	Polymer Membrane
Charge Carrier	OH^-	H^+	CO_3^{2-}	O^{2-}	H^+
Operating Temperature	60-220℃	200℃	650℃	600-1000℃	80℃
Catalyst	Platinum	Platinum	Nickel	Perovskites (Ceramic)	Platinum
Cell Components	Carbon Based	Carbon Based	Stainless Based	Ceramic Based	Carbon Based
Fuel Compatibility	H_2	H_2	H_2, CH_4	H_2, CH_4, CO	H_2, Methanol

Table 1. Types of main fuel cells.

1.2 Solid oxide fuel cell electrolyte formation technology

1.2.1 Principle of Electrolyte Thin-Film Technology

Solid oxide fuel cells are solid-state electrochemical power generation devices that directly convert chemical energy into electrical energy. However, today, solid oxide fuel cells still have many problems. Since the current is generated by oxide ions (or protons) through the solid electrolyte, achieving high ionic conductivity will lead to remarkably high operating temperature (~800-1000°C) of SOFC during operation[21]. The electrodes react with the electrolyte at high temperatures, and the fuel cell performance decreases. Moreover, the high working temperature has higher requirements on the thermal stability, high-temperature strength, electronic conductivity, thermal expansion matching, and chemical stability of each component, which increases the difficulty of material selection. Therefore, it can be seen that reducing the operating temperature of solid oxide fuel cells (SOFCs) in order to reduce costs and prolong the life of fuel cells is the most significant technical challenge for their development. However, reducing SOFC operating temperature can lead to some problems, such as ohmic drop through the electrolyte and electrode over potential. To overcome these fuel cell performance losses, reducing the electrolyte resistivity is necessary, which can be achieved by reducing the thickness of the electrolyte.

Resistivity is a physical quantity used to express the resistance characteristics of various substances. For example, under a specific temperature, the resistance of a material is:

$$R = \frac{\rho L}{A} \tag{1}$$

where ρ is the resistivity, L is the length of the material, A is the

cross-sectional area of the material, and R is the resistance value. Resistivity is related to the material and external factors such as temperature, pressure, and magnetic field. The relationship between resistivity and temperature is:

$$\rho_t = \rho_0 \left[1 + \alpha(t - t_0) \right] \qquad (2)$$

where ρ_t and ρ_0 are the resistivity at t°C and 0°C, respectively, t_0 is a fixed reference temperature (usually room temperature), and α is the temperature coefficient of resistivity, which is related to the material[22]. While reducing the thickness of the electrolyte material, the current density and output power density of the fuel cell are increased.

In order to realize the low temperature of solid oxide fuel cells and reduce the electrolyte's thickness to reduce the electrolyte's resistance, the thin-film technology of the electrolyte has been an important research content in recent years[23]. Electrolyte materials need to have sufficiently high ionic conductivity, be completely dense in structure, and meet the requirements of maintaining chemical stability, stable crystal form, and stable external dimensions in an oxidizing and reducing atmosphere.

1.2.2 Electrolyte film preparation method

According to the principle analysis, electrolyte film preparation methods can be divided into the chemical method, physical method, and ceramic powder process method. However, physical vapor deposition (PVD) and chemical vapor deposition (CVD) are the most commonly used.

The use of chemical methods to prepare electrolyte films for solid oxide fuel cells mainly includes chemical vapor deposition (CVD),

electrochemical vapor deposition, and sol-gel methods. Among them, chemical vapor deposition (CVD) includes the low-pressure type (LPCVD), atmospheric pressure type (APCVD), plasma-enhanced type (PECVD), metal-organic compound type (MOCVD), and a new type of thin-film deposition technology that has appeared in recent years——Atomic Layer Deposition (ALD)[24]. Chemical vapor deposition is a chemical reaction of reactants in a gaseous state. The growth technology of depositing a solid thin film on the surface of the substrate has many advantages, such as high purity, good density, low residual stress, and no requirement for the shape of the substrate. Chour et al.[25] used chemical vapor deposition on cerium oxide as a substrate. A 5μm yttria-stabilized zirconia (YSZ) film was deposited. The open-circuit voltage of the assembled cell was about 0.93 V at 650 °C, which met the voltage requirements of solid oxide fuel cells. Oh et al. [26] developed and studied a novel chemical solution deposition method to fabricate intermediate-temperature solid oxide fuel cells (IT-SOFCs) based on chemical vapor deposition and deposited 500 nm YSZ thin films. The results showed that at 600 °C, the open circuit was The voltage is 1.07V, and the maximum power was 425mW/cm^2 , indicating that chemical solution deposition is a feasible method to reduce the thickness of the electrolyte in fuel cells. Sasaki et al.[27] used electrochemical vapor deposition to prepare YSZ electrolyte films with a thickness of 10μm at the cathode, and the single-cell power density reached 1.55W/cm^2 . However, chemical vapor deposition method materials are expensive, the reaction temperature is high, and gas corrosion will occur during the film formation process, which still needs to be solved.

Atomic Layer Deposition (ALD), also known as Atomic Layer Epitaxy (ALE), is a thin-film deposition technology based on surface

gas-phase chemical reactions, in which substances are deposited layer by layer on the surface of a substrate in the form of a single atomic film, which is similar to ordinary chemical deposition. In the atomic layer deposition process, the chemical reaction of a new layer of the atomic thin film is directly related to the previous layer, which means that only one layer of atoms is deposited in each reaction in this way. Atomic layer deposition technology has broad application potential in nanomaterials because of the controllable deposition parameters, good deposition uniformity, and consistency. For example, Ji et al.[28]deposited a fuel cell with 40 nm thick YSZ and 420 nm thick GDC bi-layered thin-film electrolyte by atomic layer deposition, and the open-circuit voltage was 1.07 V at 450 °C, and the power density reached 35mW/cm^2.

Physical methods the methods of preparing solid oxide fuel cell electrolyte thin films mainly include the physical vapor deposition (PVD) method and spraying method. Among them, physical vapor deposition includes thermal evaporation deposition and plasma sputtering deposition. Thermal evaporation deposition is divided into resistance evaporation deposition and electron beam evaporation deposition according to different evaporation methods. Plasma deposition can be subdivided into DC sputtering, radio frequency sputtering, and magnetron radio frequency sputtering according to different plasma generation methods.

The physical vapor deposition method uses physical methods (sputtering, evaporation) to deposit materials on the surface of the substrate to form a film. The physical vapor deposition method has the advantages of rapid film formation, easy control of the film formation process, and low deposition temperature. Especially in the magnetron sputtering technique, which can use lower temperatures to produce

relatively smooth surfaces with excellent mechanical and tribological properties and excellent adhesion to the primary materials used as substrates[29]. Srivastava et al.[30]successfully fabricated dense YSZ electrolyte films on NiO-YSZ composite porous anode supported by DC magnetron sputtering in physical vapor deposition. The assembled fuel cell has an open-circuit voltage of 1.09V at 800°C and maximum output power of 600mW/cm^2. Wang et al. [31] used reactive magnetron sputtering to prepare YSZ films with a thickness of 10μm on NiO-YSZ anode substrates. A single cell with sputtered YSZ film as the electrolyte and LSM-YSZ as the active cathode material obtained an open circuit voltage of 1.08 V and a maximum power density of 700mW/cm^2 at 750 °C. In recent years, new materials have been produced in solid oxide fuel cells. For example, Sun et al. [32] successfully deposited a new electrolyte $La_{0.9}Sr_{0.1}Ga_{0.8}Mg_{0.2}O_{3-\delta}$ (LSGM) film on the anti-carbon deposition anode $La_{0.7}Sr_{0.3}Cr_{0.5}Mn_{0.5}O_{3-\delta}$ (LSCM) by radiofrequency sputtering deposition. The results proved that the new electrolyte film has high density and good electrochemical performance, confirming that the radio frequency sputtering method has a good development prospect in preparing high-performance electrolyte films in solid oxide fuel cells.
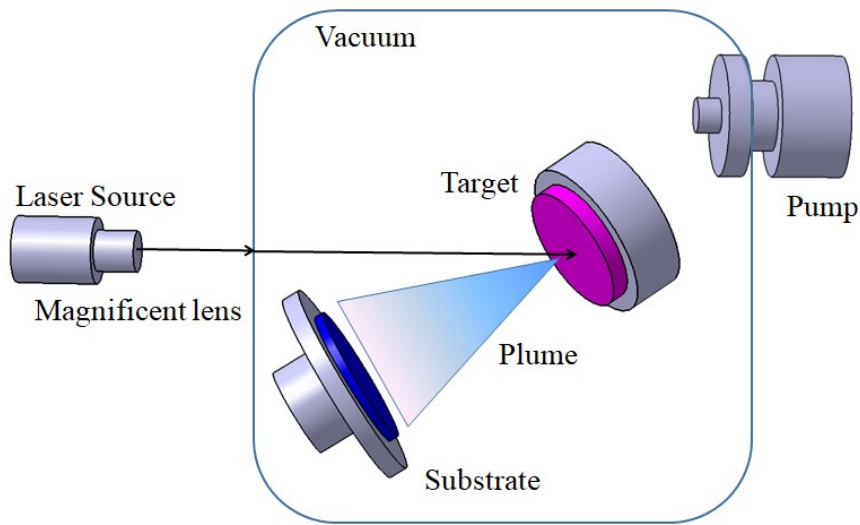
(a)Schematics of pulsed laser deposition
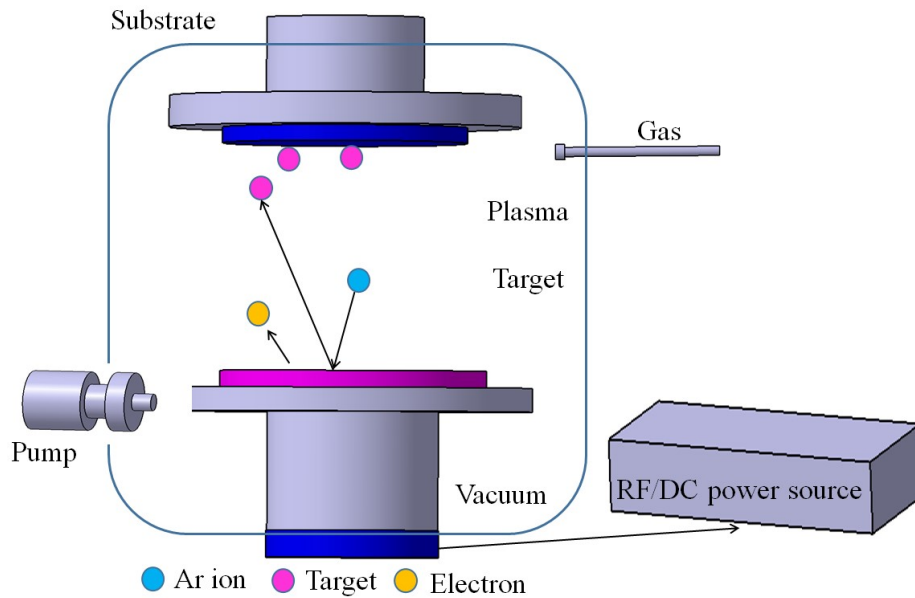
(b)Schematics of sputter

Figure 2. Schematics of physical vapor deposition processes

There are still many problems in the physical vapor deposition method, such as it is challenging to prepare thin films on surfaces with complex shapes. It is difficult to control the composition ratio of the thin films; it needs to be operated in a high vacuum state, the manufacturing equipment is complex and expensive, and the industrial preparation of solid oxide fuel cells Thin films have significant limitations.

13

In summary, there are many methods for preparing solid oxide fuel cell electrolyte membranes, and each method has its advantages and disadvantages. However, we can confirm that the current electrolyte film preparation technology is developing in the general direction of low cost, high efficiency, and large-scale continuous production.

1.3 Thin Film Solid Oxide Fuel Cells (TF-SOFCs)

Solid oxide fuel cells with electrolyte membranes are often referred to as thin-film solid oxide fuel cells (TF-SOFCs). Electrolyte thinning is one of the essential means to reduce the fuel cells internal resistance, reduce the working temperature of the fuel cell, and increase its output power. The thinner the electrolyte, the smaller the various losses the better the fuel cells performance. However, to avoid gas leakage, the electrolyte film needs to be continuous, dense, and without apparent cracks. The electrolyte membrane is located between the two porous electrodes, and the reactive gases can freely enter and exit the electrochemically reactive active sites near the electrode-electrolyte interface.
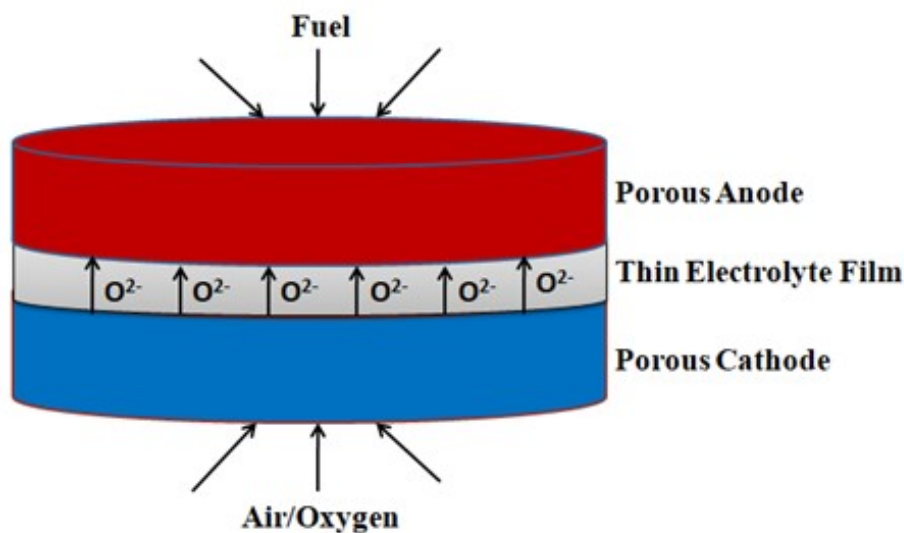
Figure 3.Schematic diagram of thin film solid oxide fuel cells (TF-SOFCs)

Different techniques are used to achieve film deposition according to different film-forming materials and different expectations for electrolyte film. Among the various film formation methods, CVD/ALD deposition and PVD deposition are the most commonly used electrolyte film formation methods. As the fuel cell's core component, the electrolyte's primary function is to conduct ions and form a conductive path between the cathode and the anode. Commonly used solid electrolytes can be divided into fluorite-type oxides, lanthanum molybdate (LAMOX) series, and perovskite-type oxide electrolytes with mixed ionic and electronic conductivity. Fluorite-type oxides are currently the most widely used electrolyte materials in solid oxide fuel cells. The fluorite structures used as SOFC electrolytes mainly include zirconia-based electrolytes（ZrO_2）, ceria-based electrolytes（CeO_2）, and bismuth oxide-based electrolytes（Bi_2O_3）[33]. Fluorite structure oxides are simple cubic lattices composed of anions in a face-centered cubic close-packed cation lattice, anions occupy all tetrahedral voids, and all octahedral voids are empty. Diffusion in the lattice provides transport channels.

Yttria-stabilized zirconia (YSZ) is a commonly used electrolyte material for SOFCs. However, due to pure zirconia's poor oxygen ion conductivity, doping is usually used to improve conductivity. The primary doping materials are CaO, MgO, Sc_2O_3, Y_2O_3 and some rare earth oxides. Although the electrical conductivity of YSZ is not the highest, it is widely used in the preparation of thin films due to its good redox stability, low price, and sufficiently high oxygen ion conductivity at high temperatures [34].

Ceria-based electrolytes have high electrical conductivity. However, the traditional electrolyte material YSZ leads to low ionic conductivity with the decrease of operating temperature, and the conductivity of

cerium-based electrolytes at low temperature has more potential. Sm, Gd (SDC, GDC) as doping materials have extremely high electrical conductivity. The reason is that the larger ionic radius produces a broader structure, which is conducive to the migration of oxygen ions. However, electrolytes such as GDC have some limiting factors, such as narrow working temperature range, unstable under low oxygen partial pressure, and reducing atmosphere. Ce^{4+} in the electrolyte is easily reduced to Ce^{3+}, and electronic conductance occurs deteriorates the electrical properties of the material. At the same time, during the reduction process, Lattice expansion is easy to crack difficult to sinter molding. In order to improve the chemical and mechanical stability of GDC and reduce OCV loss under reducing conditions, an effective method was reported to add YSZ as a barrier layer between GDC and anode to suppress the chemical reduction and current leakage of GDC [35], [36].

Solid electrolytes are crucial in the development of low-temperature SOFCs. Doping and improving existing electrolytes is a standard method to increase the concentration of oxygen vacancies, improve ionic conductivity, and reduce the operating temperature of batteries. For example: $La_{0.9}Sr_{0.1}Ga_{0.8}Mg_{0.2}O_{3-\delta}$ (LSGM) electrolyte has been demonstrated[37] to increase the maximum power density of SOFC to $0.612W/cm^2$ at 500 °C. Ahn et al.[38] studied the $Sm_{0.075}Nd_{0.075}Ce_{0.85}O_{2-\delta}$(SNDC) electrolyte, and the maximum power density of the fuel cell was increased to $0.32W/cm^2$ under the operating condition of 500 °C.

At present, the research on electrolytes is still in the early stage of development. The main problem to be solved is to improve the ionic conductivity of electrolyte materials and, at the same time, improve the chemical stability and avoid redox.

1.4 Anodized aluminum oxide (AAO) supported thin-film solid oxide fuel cells (TF-SOFCs)

In order to fabricate better-performing thin-film solid oxide fuel cells (TF-SOFCs), unique thin-film-supporting substrate materials need to be selected to complement their lack of mechanical strength. According to the choice of different substrate materials, the types of TF-SOFC are also different. The commonly used substrates are silicon wafer, porous metal plate, anode particles, and anodized aluminum oxide (AAO).

The silicon wafer applied on TF-SOFC is not supported by silicon in nature, which itself is called freestanding. The production process is to etch the silicon after the entire thin-film element is fabricated on it. Its purpose is to remove the phosphosilicate glass layer on the backside of the substrate to prevent short circuits from occurring. Post heat treatment is possible due to the post-etch process and lower thermal expansion coefficient of silicon. Due to the relatively excellent step coverage of the thin-film fabrication method, the pores at the nanoscale are maximized to fabricate dense electrolytes. For example, Huang et al.[39] fabricated a freestanding SOFC film with a sputter-deposited 50 nm-thick YSZ film on a Si substrate and achieved a peak power density of $130 mW/cm^2$. Therefore, anode particles always require anode functional layers to stack thin-film anodes and electrolytes due to their large pores (on the order of several micrometers) and tortuosity. For the same reason, porous metal plates have the same problem. Despite its electronic conductivity, wide scalability, and solder ability, it is not widely used to support fuel cells due to its high thermal expansion coefficient and randomly distributed macro pores.
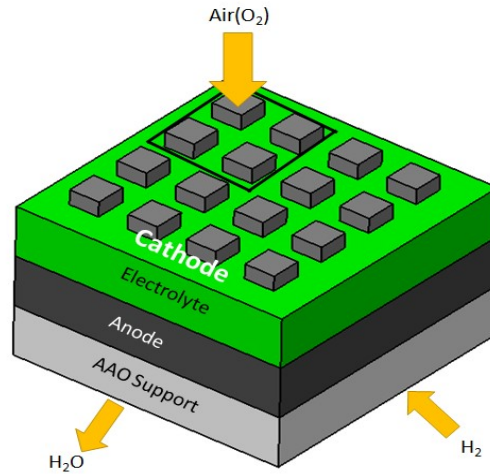
Figure 4. Schematic image of AAO supported thin film solid oxide fuel cells

Anodized aluminum oxide (AAO) is a honeycomb structure with a high-density uniform and parallel pores array. The size of the reactive pores can be controlled from a few nanometers to several hundreds of nanometers, and dense electrolytes can be deposited by PVD, ALD, and other methods. In thin films, the porosity of AAO substrates enables high-density thin films to fabricate porous electrodes. In addition to good thermal and mechanical stability[40] , the thermal expansion coefficient is similar to that of SOFC electrolytes. Therefore, AAO was used as the support material to fabricate TF-SOFC in this study, considering the above characteristics.

In order to fabricate stable and high-performance TF-SOFCs, various studies have been carried out on AAO-supported TF-SOFCs. We usually employ CVD/ALD to fabricate fully dense films with high coverage to address electrolyte defects due to nanopore arrays of AAO. Ji et al.[41] utilized plasma-enhanced ALD (PEALD) to deposit a 70-nm-thick YSZ electrolyte and successfully achieved an open-circuit voltage of 1.17 V and a power density of $170mW/cm^2$ at 500 °C. Meanwhile, Ha et al.[42] used a combination of atomic layer deposition and sputtering to deposit dense YSZ electrolytes. Using this combined deposition method, a YSZ electrolyte with a total thickness of about

390 nm was successfully fabricated on porous AAO. The cell's open-circuit voltage with this electrolyte was verified to reach 1.14 V at 350 °C in an atmosphere of pure hydrogen and ambient air.

Most of the cathodes of AAO-based thin-film SOFCs are fixed on the noble metal platinum to ensure an appropriate redox reaction (ORR) rate due to the lower operating temperature [39], [43]. To overcome the poor thermal stability of platinum, a thin ceramic film layer can be introduced on the cathode. Hong et al.[44] fabricated GDC capping layers on metallic platinum cathodes by sputtering to improve thermal stability and redox reaction (ORR) kinetics by varying the thickness of the films on platinum cathodes, on AAO substrates A heat-resistant low-temperature solid oxide fuel cell (LT-SOFC) was fabricated, demonstrating the enhancement of fuel cell performance and the thermally stable behavior of the GDC capping layer. The enhanced peak power density is 258mW/cm^2 , and the degradation rate of the platinum cathode is 56.4% after operating at 450 °C for 25 hours. The anode structure of AAO-based TF-SOFC fuel cells has also been studied. The enlargement of the three-phase boundary (TPB) is the key to performance improvement, and the anode structure has been optimized in various ways. Li et al.[45] investigated the possibility of using nickel-based anodes as an alternative to platinum anodes for TF-SOFCs operating at low temperatures. A mixed gas of argon and oxygen is used to oxidize the particles sputtered from the Y-Zr metal alloy during the sputtering process. To ensure the electronic conductivity of the anode, dense Ni was sputtered first, and then Ni-YSZ was deposited. The peak power density at 500 °C of the Ni/Ni-YSZ bilayer anode prepared by the co-sputtering method is about 37% higher than that of the optimized platinum anode, proving that the nickel-based anode in low-temperature SOFC can replace the noble

metal anode. The ohmic resistance continued to decrease with the thickening of the nickel film anode. However, the Faradaic resistance has an optimal value because the reaction area can be maximized depending on the anode's thickness and pore conditions. These resistive properties allow the optimal combination of AAO pore size and Ni anode thickness to be found[46]. Yu et al.[47]significantly improved the in-plane connectivity of nanostructured nickel anodes by controlling the substrate's sputtering film-forming angle and rotational speed. As a result, the optimized nickel anodes achieved $477\mathrm{mW/cm^2}$ performance at 500 °C, which is an excellent result of anodization—best-recorded performance of an aluminum-supported nickel-based TF-SOFC.

1.5 The main research content of this paper

In this study, sputtering was used to fabricate dense electrolytes to improve the performance of thin-film solid oxide fuel cells. As a result, the sputtering coating has many advantages such as high deposition ion energy, good film adhesion performance, high film density and low impurity content, controllable film thickness, and the ability to prepare large-area films[48], [49]. By changing the parameters of sputtering conditions (sputtering pressure, sputtering power, distance from the target to the substrate), the influence of the parameters on the electrolyte film is studied, and the electrolyte film is as thin as possible (about 1um) is produced. The resistance of the fuel cell is changed. Resistance is reduced to a minimum. At the same time, the residual stress and the morphological changes of the film were analyzed during the process. The change of the sputtering pressure means that the film morphological and residual stress changed. (The content of the

subsequent chapters is explained), the content and contributions described in each chapter will be summarized below:

Chapter 2 shows the development of the electrolytic reactive sputtering process by changing different experimental and sputtering parameters to study the effect on the nanostructure of electrolyte films in order to find the best conditions for obtaining high-quality electrolyte films. With the increase of sputtering pressure, the grains gradually showed a neat columnar arrangement, and the surface roughness of the film increased. Among them, the YSZ thin-film electrolyte layer prepared under the sputtering pressure of 3mTorr showed a higher density.

Chapter 3 uses XRD to study thin films' crystalline and residual stress prepared under different sputtering pressures. By using Bragg's law, the lattice spacing is calculated, and the existence of residual stress is proved. The results show that with the increase of sputtering pressure, the peak angle increases, and the stress state of the film changes from compressive stress to tensile stress. The film prepared under the sputtering pressure of 3mTorr exhibits compressive stress, and the existence of compressive stress makes the grains move toward denser ones. In the direction of growth, the electrolyte film is more compact.

Chapter 4 the electrochemical analysis is an effective method for new energy fuel cells to characterize the electrochemical performance. For example, it was found that the electrolyte film prepared under the sputtering pressure of 3mTorr has an open circuit voltage (OCV) of 1.043 V and a maximum power density of $1.593 W/cm^2$. Moreover, using electrochemical impedance spectroscopy (EIS) to measure the impedance change with the frequency of the sine wave, analyze the electrode process kinetics, electric double layer and diffusion, and study electrode materials' working mechanism solid electrolytes.

CHAPTER2. Sputtering Conditions and Nanostructures

2.1 Introduction

The application of sputtering thin film materials is extensive. The adhesion of the thin film is an essential factor affecting the quality of the thin-film material, and the bonding strength of the thin film and the substrate is one of the keys restricting the practical application of thin-film materials. Different sputtering conditions have different effects on the adhesion performance of the film. The adhesion performance is a key factor restricting the performance and reliability of the sputtered film. With the continuous improvement and development of sputtering technology, the adhesion performance of the film has improved. Specific to the performance of various films and substrates, the sputtering conditions of the sputtering process play an important role, and the sputtering conditions have become an essential factor affecting the adhesion performance of the films and substrates. High-quality thin film research and development have been widely concerned about changing specific sputtering conditions. For example, Xiao et al. [50] used electron beam evaporation technology to control technical parameters such as deposition rate and oxygen partial pressure. They deposited YSZ thin films on borosilicate glass substrates. The conclusion is obtained through experiments; when the deposition rate is $0.4\mathrm{nm/s}$, and the oxygen pressure is $2.0 \times 10^{-2}\mathrm{Pa}$, the YSZ film with the best performance is obtained. Meng et al. [51] investigated the effect of RF magnetron sputtering parameters on the structure and properties of SiC thin films. In addition, the effects of

improving the distance from the target to the substrate, sputtering power, deposition pressure, substrate temperature, and bias voltage on the structure and properties of SiC thin films were investigated. Finally, a film with a high elastic modulus (310.8Gpa) and hardness (35.6Gpa) was obtained. SiC films demonstrate that high-performance and high-quality films can be obtained by changing the sputtering parameters.

In all branches of material science, the development of nano-film material science occupies a critical position [52], [53]. Nano-film refers to a film composed of crystal grains (or particles) with a size in the nanometer scale or a composite film composed of nanocrystal grains embedded in a particular film. The properties of nanofilms strongly depend on the grain size, film thickness, surface roughness, and structure of the multilayer film. The following describes the characterization of thin films. Generally, thin-film materials are not processed from bulk materials but are deposited or prepared on the surface of bulk materials by unique methods. Thin-film materials are valued because they often have unique properties or combinations of properties. Thin films vary in morphology and structure, depending on their constituent materials, film-forming methods, and desired functions. Therefore, the structure and composition of the film must be analyzed in a certain way. The performance of the film depends on the composition structure of the film. The research on the film structure can be divided into three levels according to the scale studied:

(1) The macroscopic morphology of the film, including the film size, shape, thickness, uniformity;

(2) The microstructure of the film, such as the size and distribution of grains and phases, pores and cracks, interfacial diffusion layer and film texture;

(3) The microstructure of the film, including grain defects, grain boundaries Integrity of the interface with epitaxy, dislocation configuration [54].

The microstructure and morphology of the thin film material are mainly observed, including the surface morphology, the interlayer morphology of the thin film, the interface with the substrate, and the fracture morphology. The purpose of the observation is to understand the microstructure, interface structure, defects, grain size of the thin film material. Moreover, through further analysis, the thin film material's growth mechanism, mechanical properties, and physical properties were studied.

By studying the growth process of thin films, obtaining high-quality thin-film materials has received extensive attention[55], [56]. The growth process of the thin film can be divided into two stages, namely the row nucleus of the new phase and the growth stage of the thin film. The so-called formation stage of the film's core refers to the initial stage of film formation when some gaseous atoms or molecules begin to condense on the surface of the substrate. The so-called growth stage of the film means that the atoms on the surface of the substrate first form groups of atoms that can move, referred to as "islands," and then these tiny islands gradually grow and merge, and finally form a continuous film on the substrate. For many combinations of thin films and substrates, as long as the deposition temperature is high enough and the deposited atoms have a certain diffusivity, the growth of the thin film shows an island growth mode; when the wettability between the deposited material and the substrate is good, the atoms of the deposited substance are more inclined to bond with the atoms of the substrate, and the film growth shows a layered growth mode; in the layered-island growth mode, after the initial layered growth of one or

two atomic layers, the growth mode Convert from layer growth mode to island growth mode. The isolated core formed in the initial stage of film nucleation will gradually grow over time. This process involves not only the absorption of single gas-phase atoms and surface adatoms but also the process of mutual engulfment and combination between the cores [57].
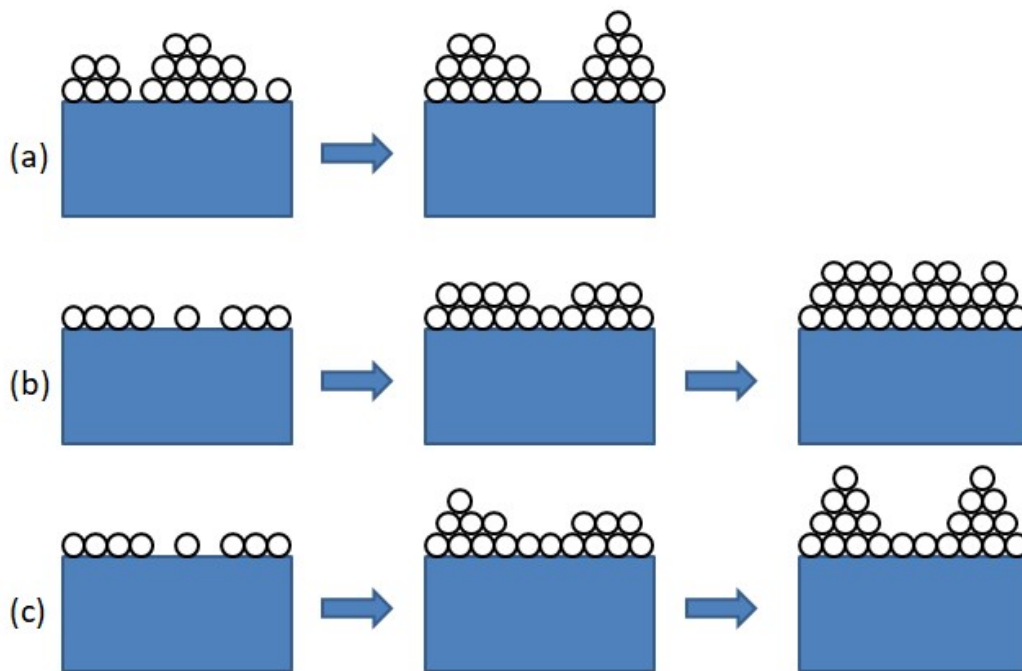
Figure 5. (a) Island growth mode (b) Layered growth mode (c) Island-layered, film growth diagrams under three growth modes

In the deposition process of the film, the incident gas molecules (atoms) usually go through three processes, namely, the adsorption process on the surface of the substrate or film; diffusion on the surface of the substrate or film, some atoms are detached from the attachment, and another part of the atoms are on the surface of the film Some low-energy site deposition process; sufficiently high substrate temperature, atomic diffusion process inside the film. Therefore, according to different deposition conditions, the thin film structure prepared by the sputtering method will show different structure

morphologies.

In this chapter, YSZ and GDC electrolyte films are prepared by sputtering by physical vapor deposition. By changing the sputtering pressure, the distance from the target to the substrate, the gas flow rate, the power of RF sputtering and magnetron sputtering in order to obtain the best sputtering parameters, the nanostructure changes during the sputtering process of the thin films were studied and observed.

2.2 Experimental

2.2.1 Properties and Experimental Procedures of Thin Films

In this experiment, YSZ (3N, 99.9% pure) target, GDC (3N5, 99.95% pure) target, and Ni (4N, 99.99% pure) target, the targets used in the above experiments are all produced by VTM (Vaccum Thin-film Materials, Korea). The experimental gases were argon (with a concentration of 99.999%, produced by DEOKYANGGAS) and oxygen (with a concentration of 99.995%, produced by DEOKYANGGAS). Scanning electron microscopy (SEM) was used to analyze the differences in the electrolyte surface and cross-sectional area of nanostructures as a function of deposition conditions. In addition, crystallinity and film stress was measured and analyzed using X-ray diffraction (XRD).

In this experiment, the physical vapor deposition technique was used, and a commercial sputtering machine (Korea Vacuum Tech Systems Co, Ltd.) was used to prepare the ultrathin electrolyte membrane, which resulted in good coverage. A highly commercialized AAO (Research and Development, Korea) template was used as the substrate to take advantage of its high density of nanopores and the resulting

electrochemical reaction sites[43], [58]–[60].Nickel-based anodes have the potential to be an alternative to platinum anodes for TF-SOFCs operating at low temperatures with higher power densities[45]. Platinum electrodes have very stable chemical properties and are widely used as cathode materials by many researchers[61], [62].

The deposition process was carried out at room temperature. First, the Ni anode was deposited by DC sputtering on the AAO template. The argon gas flow was set to 50 sccm, the sputtering power was 200 W, and the sputtering was performed for 30min. Then, the radio frequency magnetron sputtering technology was used on the Ni anode deposit YSZ electrolyte. YSZ electrolyte was deposited with different sputtering pressures (3mTorr, 5mTorr, 10mTorr, 20mTorr), the deposition time was 9h, the gas flow of argon was set to 50sccm, the sputtering power was 75W, four experimental groups of YSZ thin films prepared under different sputtering pressures were obtained under the above experimental conditions. After the sputtering of each group of YSZ films is completed, use a cleaning machine to purge the sputtering chamber to ensure that there is no impurity dust in the sputtering chamber. Finally, a platinum cathode was deposited on the sputtered YSZ layer by DC magnetron sputtering, the argon gas flow was set to 50sccm, and the sputtering power was 100W. A solid oxide thin-film fuel cell comprises of layers and a platinum cathode.

Using the same method, GDC was deposited on a silicon wafer with different pressures (5mTorr, 10mTorr, 20mTorr, 50mTorr), and the magnetron sputtering power was 100W, and then YSZ was deposited for two hours. After that, the GDC electrolyte was sputtered on YSZ, Also prepared under different sputtering pressures (5mTorr, 10mTorr, 20mTorr, and 50mTorr) to form a bilayer electrolyte film. Next, a 30min Ni electrode was deposited under the sputtering power of 200W

and the pressure of 50mTorr, and a 5min platinum electrode was deposited under 100W and 50mTorr. Sputtering YSZ electrolyte at different powers (100W, 65W, 50W) .And the difference between the sputter-deposited YSZ on the AAO substrate and the sputter-deposited YSZ on the silicon substrate was observed to compare the difference in structure and properties of the two films. In the same way, the sputtering pressure was set at 10 mTorr and the sputtering power was 50 W, and the GDC electrolyte was sputtered and deposited. The sputtering time was 4 h. The electrolyte structure was observed by changing the distance from the target to the substrate (28 cm, 30 cm).

2.2.2 Electrochemical evaluation

First, set up a base material that can accurately place the experimental group, connect the four sides of the base with silver wires(0.5 φ) , use Silver Conductive Link Liquid (S-020, USA) to bond the silver wires and the base, and put it into the electric furnace (operating voltage 220V, current 5.5A, electric power 5kW, Korea) was heated for 30min to 200°C, and then maintained at 200°C for 10min, in order to fully bond the silver wire to the substrate. Subsequently, Ceramabondpowder and Ceramabondliquid were mixed in a ratio of 1:1.2 to 1.3 to obtain a ceramic binder (571-P, AREMCO, Korea) with a weight of about 1 g. The obtained experimental group was placed on the substrate after completing the experiment. The test cell was bonded to the test substrate with a ceramic adhesive and connected with the silver wire. Then the surrounding was sealed and bonded to prevent hydrogen gas from being exposed. Heat to 500°C then using an electric furnace machine. Then, dry hydrogen gas (concentration 99.999%, produced by DEOKYANGGAS) was introduced into the anode side

with a mass flow of 10~15sccm, the cathode was exposed to the atmosphere, and an electrochemical test system (Interface1000, Potentiostat/Galvanostat/ZRA, Gamry, USA) was used. Finally analysis of the polarization of thin-film fuel cells.

Figure 6. Commercial Sputtering Machine
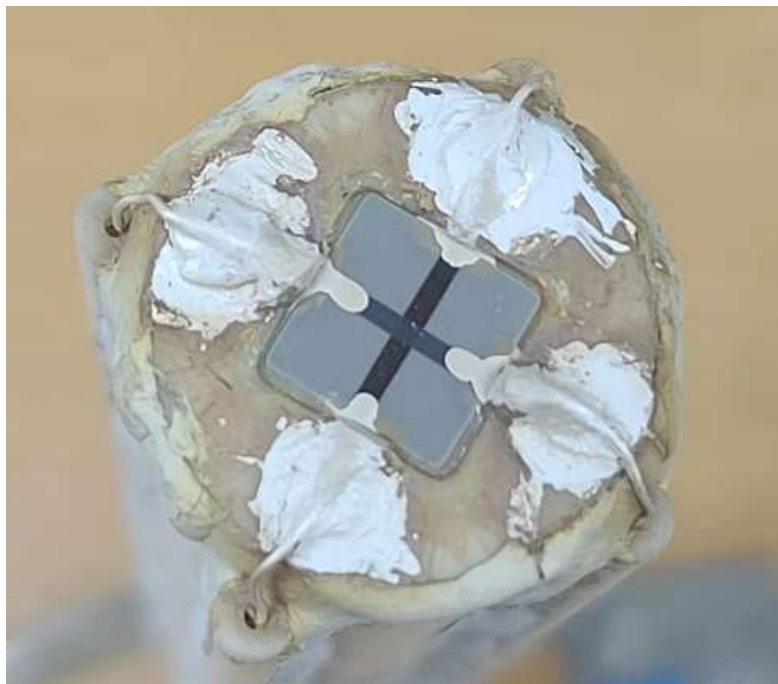
Figure 7. Electrochemical testing

2.3 Result & Discussion

2.3.1 Effect of Sputtering Pressure on Electrolyte Thin Films

In order to characterize the effect of preparing the electrolyte under different sputtering pressures, the GDC electrolyte was firstly sputtered onto the silicon wafer substrate by magnetron sputtering. The sputtering power was set to 100W, and The SEM cross-sectional image is shown in Figure 8. From the figure, we can see that as the sputtering pressure increases, the crystalline state of the sputter-deposited film becomes more apparent. From the change from 5mTorr to 50mTorr, it can be seen that at higher sputtering pressure, the section of the deposited film has prominent columnar grains, and at 50mTorr, neat and dense grains with a height of about 824 nm and a width of about 0.034μm are formed. It can be seen from the figure that the change from 5mTorr to 20mTorr is not apparent, but comparing the interface diagrams of 5mTorr and 50mTorr sputtering pressures, we can find that there is apparent columnar grain growth. As the sputtering pressure increases, the film thickness (shown in Figure 8) increases before decreasing. When the working gas pressure is low, the film thickness increases with the increase of the sputtering pressure, mainly due to the increase in the number of argon ions bombarding the target at the same power and the increase of atoms sputtered from the target. The film deposition rate increases. At the same time, the density of gas molecules in the vacuum chamber increases, and the mean free path of particles decreases. Therefore, the probability and number of collisions between the sputtered target atoms and gas molecules increase. As a result, the probability of reaching the substrate and attaching to it decreases, hindering the deposition of thin films. As the sputtering pressure

continues to increase, the effect of the collision between the sputtered atoms and the gas molecules occupies a favorable situation so that the film deposition rate decreases and the thickness become smaller within the same deposition time.

Figure 9 shows the surface images of the thin films under sputtering pressures of 5mTorr and 50mTorr. The figures show that the higher the sputtering pressure, the relatively neatly arranged grains and the more refined the particles. Under the working pressure of 5mTorr, an "island"-like crystal nucleus with a size of about 50nm was generated. Some islands will merge and grow with the arrival of deposited atoms, while some islands cannot merge, leaving gaps between islands. As a result, the film's surface looks like a network structure or a channel structure, and the internal defects of the film increase. With the gradual increase of the sputtering pressure, the high pressure is favorable for the growth of the film in the vertical direction. Under the sputtering pressure of 50mTorr, the surface presents a flatter structure with finer particles.

In the initial stage of atoms reaching the surface of the substrate, some uniform, small and mobile atomic groups, called "islands", are first formed on the substrate. At the beginning of sputtering, these small islands, like liquid droplets, continue to accept new deposited atoms and merge with other small islands to grow gradually. The number of islands will quickly reach saturation. While the island merging process progresses, new islands are formed on the vacated substrate surface. This process of island formation and merging continues until the isolated islands are connected to each other, leaving only isolated holes and channels that are continuously filled with later deposited atoms. While the voids are being filled, a structurally continuous film is

formed. The process of island merging usually continues until the film thickness reaches a certain level.

During polycrystalline thin film growth, the development of aligned columnar structures is a natural consequence of the van der drift faceted growth model[63]. In this model, randomly oriented nuclei grow competitively on the substrate. These crystallites, whose fastest-growing direction is perpendicular to the substrate plane, grow higher and gradually wrap less favorable crystallites. Van der Drift called it a "survival model for the fastest growing crystallites".

During the film formation process of the sputtering method, the ions and high-energy neutral particles incident on the surface of the substrate has a significant influence on the surface of the substrate, which can make the surface of the substrate rough, ion implantation, quick charging of small islands on the surface, and Chemical reactions generation of residual gas molecules. The nucleation conditions have apparent changes, the formation process of nucleation centers is accelerated, and the nucleation density is significantly increased. As a result, there are many opportunities for impurity gases or external materials to be incorporated into the film, and chemical reactions such as activation or ionization are likely to occur. In addition, due to the enormous kinetic energy of the incident ions, the temperature changes of the substrate and the film are also relatively significant.
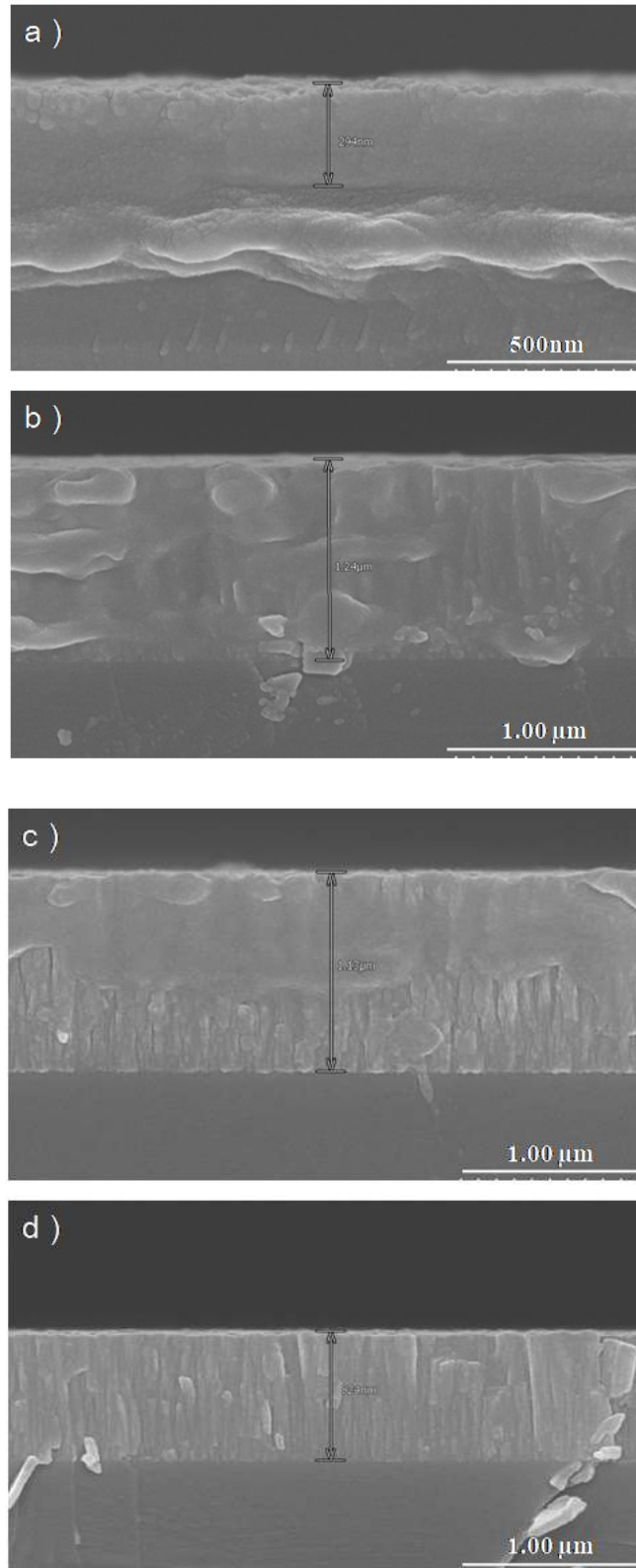
Figure 8. SEM cross-sectional images of GDC electrolytes deposited on silicon substrates at (a) 5mTorr, (b) 10mTorr, (c) 20mTorr and (d) 50mTorr sputtering pressures.

33
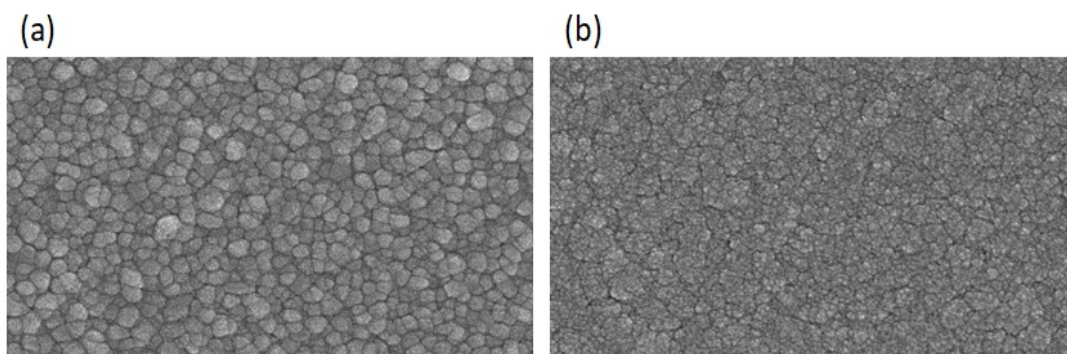
Figure 9. (a) 5mTorr (b) 50mTorr surface SEM image under sputtering pressure.

Then we studied the effect of sputtering pressure on the double-layer electrolyte. First, the YSZ electrolyte was sputtered at a sputtering power of 100W for 2h; the GDC electrolyte was sputtered on the deposited YSZ electrolyte. The SEM cross-sectional images of different sputtering pressures As shown in Figure 10. The YSZ electrolyte layer deposited by sputtering is about 498 nm, and YSZ has pure oxygen ion conductivity. Therefore, the electronic conductivity of GDC can be effectively reduced by adding a YSZ electron blocking layer thin-film structure to the GDC material. It can be seen from the figure that when the sputtering pressure is 5mTorr, there is a clear layer-to-layer boundary between YSZ and GDC. This is because the atoms deposited at the beginning of sputtering carry relatively high energy and have specific surface diffusion ability. However, due to the relatively low temperature of the substrate and the high air pressure, the energy carried by the atoms themselves is not sufficient for sufficient diffusion. Therefore, each grain competes for epitaxial growth to form fibrous columnar crystals. Subsequent atoms grow epitaxially based on the YSZ film, maintaining a specific crystallographic relationship with the YSZ film. At the same time, the atoms are the basis of the GDC film.

Epitaxial growth occurs on the surface, resulting in a uniform columnar crystal structure.

The layer spacing will no longer be evident with the continuous increase of sputtering pressure. When the sputtering pressure reaches 20mTorr, both YSZ and GDC show noticeable columnar grains. When the sputtering pressure increases to 50mTorr, some islands and islands are Merged and interconnected. With the increasing sputtering pressure, the aligned columnar grain structure of the GDC electrolyte layer gradually formed, but the columnar grains produced under the sputtering pressure of 50mTorr merged again because of the limiting factor of the GDC electrolyte itself; it is not stable under low oxygen partial pressure and reducing atmosphere, and is prone to lattice expansion and cracking during the reduction process. The higher sputtering pressure is conducive to the growth of crystals in the vertical direction, the presence of gas increases, the gas concentration increases, the mean free path of sputtered atoms is shorter, and the preferred orientation of atoms is not apparent, showing neat vertical growth.
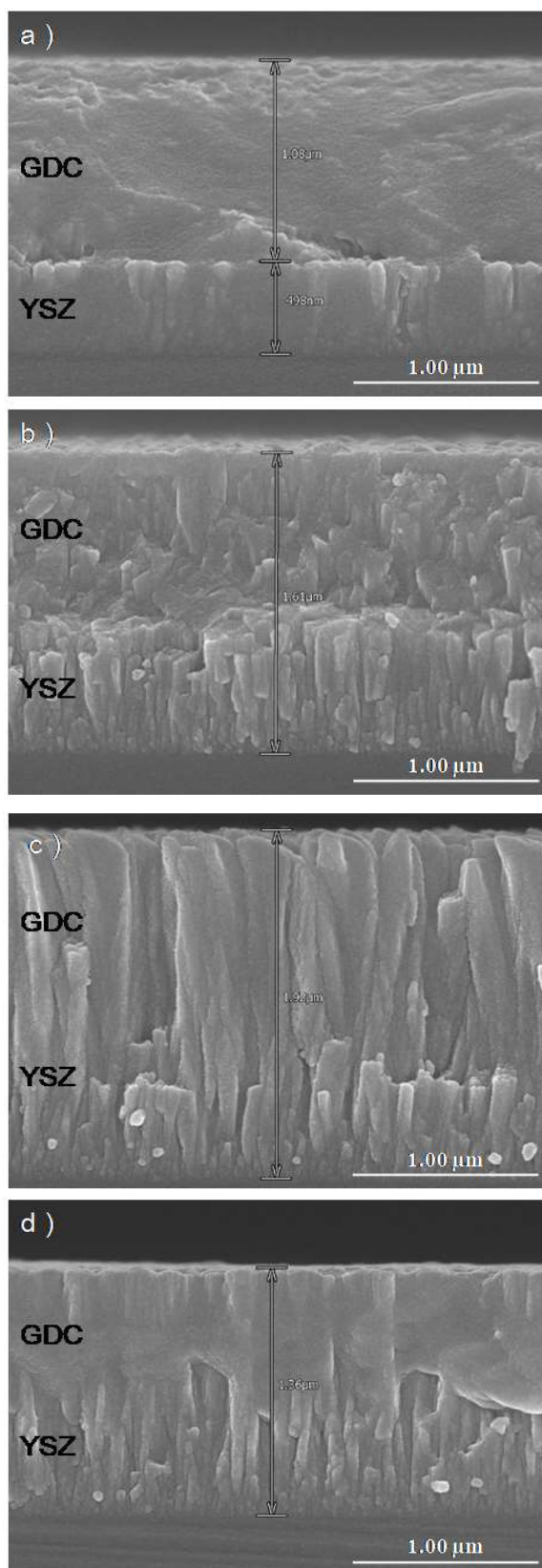
Figure 10. SEM cross-sectional images of GDC electrolytes deposited on YSZ electrolyte layers at sputtering pressures of (a) 5mTorr, (b) 10mTorr, (c) 20mTorr and (d) 50mTorr.

Due to the better redox stability of YSZ electrolyte, YSZ electrolyte was applied to AAO-supported SOFCs composed of Ni anode and Pt cathode, ensuring that the remaining sputtering parameters were the same, changing the sputtering pressure, and studying the effect of sputtering pressure on AAO loading effects of SOFCs.

The surface structure and cross-sectional structure of the electrolyte films prepared under different sputtering pressures were analyzed by SEM observation. Figure 11 shows the cross-sectional morphologies of YSZ thin films prepared under different sputtering pressures. Through SEM observation, it is found that the film layer is closely combined with the substrate and has a columnar structure perpendicular to the surface of the substrate. The thin film deposition rate of sputtering coating is generally faster, and the thin film growth shows three-dimensional island growth. The continuation of the deposition process interconnects the islands into a network, resulting in a relatively flat film. After the continuous polycrystalline thin film is formed, each crystal grain grows with the increase of the film thickness, forming the columnar crystal structure of the thin film.

It can be seen from figure 11 that with the increase of sputtering pressure, the thickness of the film increases, and the columnar structure of the crystal grains becomes more apparent. Under the sputtering pressure of 3mTorr, Ni anodes of 700~800nm were prepared. A thin film solid oxide fuel cell comprises a 2.20μm YSZ electrolyte layer and a 162 nm Pt cathode. With the increase of sputtering pressure, the number of argon ions bombarding the target material increases, the atoms sputtered from the target material increase and the film deposition rate increases. Under the lower sputtering pressure, the number of collisions between the sputtered atoms and gas molecules is reduced. The energy loss is slight, which improves the diffusion ability

of the deposited atoms and the substrate, thereby improving the density and adhesion of the film.

The typical columnar structure is not apparent from the cross-sectional images of the YSZ electrolyte prepared under the sputtering pressure of 3mTorr. The reason is that the lower the sputtering pressure, the less gas there is, the longer the mean free path of the sputtered atoms, and the more energy the atoms have to grow in the preferred orientation, so the 3mTorr grains are denser. However, under high sputtering pressure, as shown in the crystallization conditions of 10mTorr and 20mTorr films in Figure 11, the number of gas present increases, the gas concentration increases, and the mean free path of sputtered atoms is shorter, and the preferred orientation of atoms is not apparent and grows neatly upright.
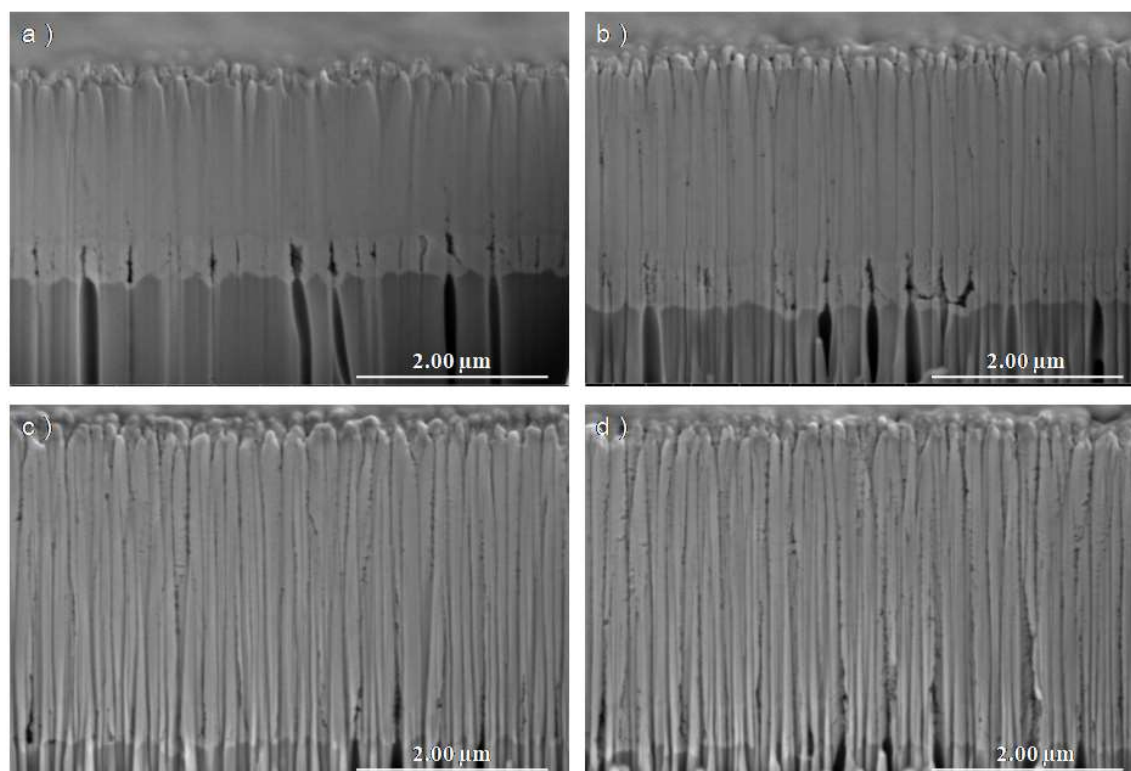
Figure 11. SEM cross-sectional images of YSZ electrolytes deposited on AAO substrates at (a) 3mTorr, (b) 5mTorr, (c) 10mTorr and (d) 20mTorr sputtering pressures.
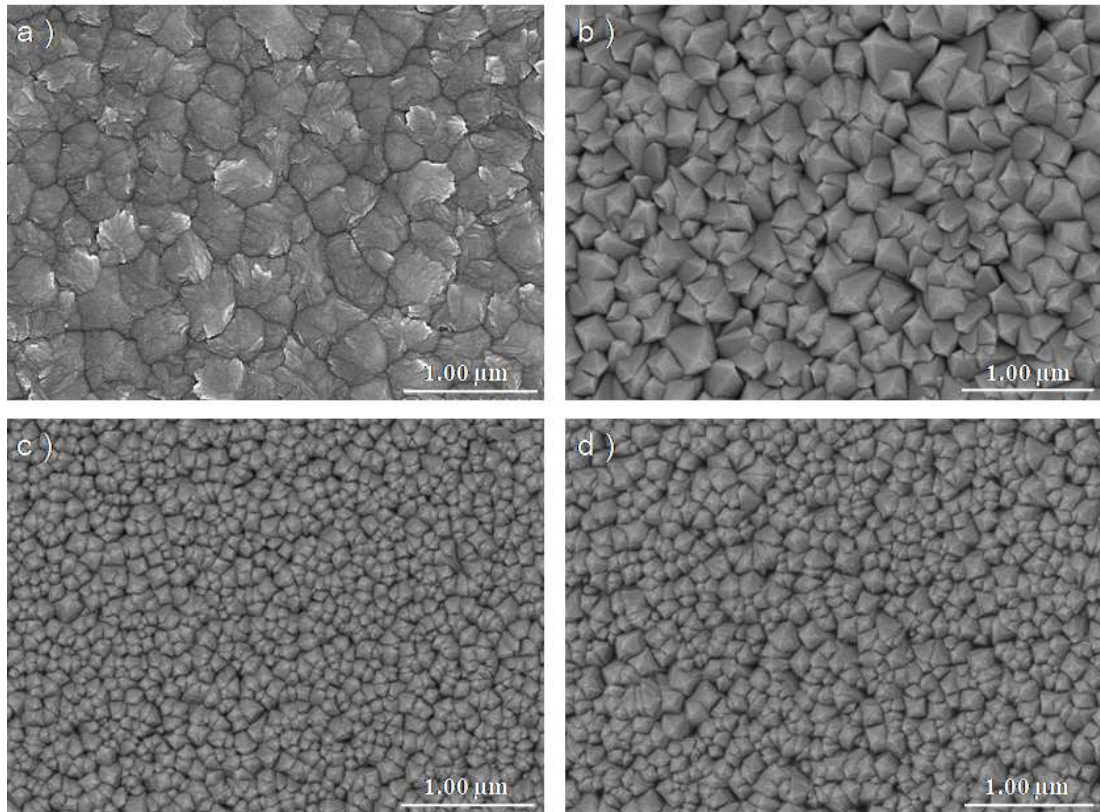
Figure 12. SEM surface images of YSZ electrolytes deposited at (a) 3mTorr, (b) 5mTorr, (c) 10mTorr and (d) 20mTorr sputtering pressures

The surface morphologies of YSZ films deposited under different sputtering pressures were observed by SEM, and the results are shown in Figure 12. With the increase of sputtering pressure, the surface roughness of the film gradually becomes coarser. Compared with 5mTorr, 10mTorr and 20mTorr, the surface image of 3mTorr has no irregularly shaped protruding islands, and the grain growth is denser. With the increase of sputtering pressure, the density of the film surface decreases, and the crystal grain gap increases. This is because when the sputtering pressure is high, the probability of collision between atoms increases; not only does the average kinetic energy of sputtered atoms decreases, but when they reach the substrate, the mutual bonding force between particles is weak, the ability of atomic migration is reduced, the structural integrity of the film is reduced and the deterioration, defects increase; the horizontal component of the sputtering atomic

velocity increases, and the deposition atomic horizontal velocity increases, resulting in a decrease in the probability of filling into the surface valleys, so films deposited under more extensive sputtering pressure conditions the surface is rough, and the particle gap increases.

2.3.2 Influence of Sputtering Power on Electrolyte Thin Films

In order to characterize the effect of electrolytes prepared under different sputtering powers, nickel anodes were first sputtered for 30 min under the conditions of sputtering power of 200 W and sputtering pressure of 50mTorr. Next, the platinum cathode was sputtered for 5 min under the condition of sputtering power 100W and pressure 50mTorr. Then, the sputtering pressure was set to 5mTorr and the sputtering time was 6h to deposit the YSZ electrolyte film by sputtering. The influence on the YSZ electrolyte film was studied by changing the sputtering power.

The cross-sectional images of the sputtered YSZ electrolyte under different sputtering powers are shown in Figure 13. It can be seen from the figure that the thicknesses of the YSZ films formed by sputtering are 1.39μm and 1.02μm, and 523nm when the remaining sputtering conditions remain the same. The film thickness gradually increases with the increase of sputtering power. Under certain conditions, the increase of sputtering power will increase the ionization degree of the discharge carrier, such as argon, increase the density of ions, increase the sputtering rate, and make the sputtered ions have higher energy, thereby improving the thin film or the adhesion of the substrate and the density of the film. On the contrary, when the sputtering power is too low, the ion density is low, the deposition rate is slow, and the ion energy is low, the obtained film has a loose structure.
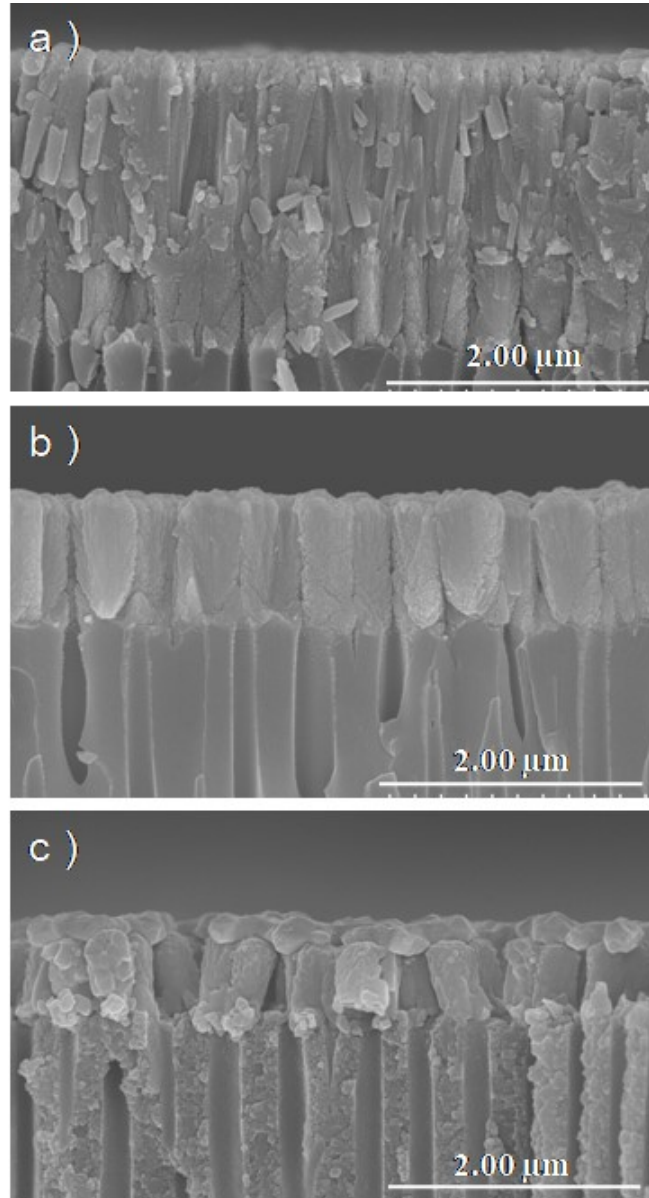
Figure 13. SEM cross-sectional images of YSZ electrolytes deposited at sputtering powers of (a) 100W (b) 65W and (c) 50W.

In the experiment, with the continuous increase of the sputtering power, the density of the incident ion current increases, the energy increases, and the sputtering coefficient also increase. According to the sputtering rate formula R=KSJ, the sputtering rate R and the sputtering coefficient S. It is proportional to the product of the incident ion current density J (K is the structure factor), so with the continuous increase of

the sputtering power, most of the sputtered particles have high energy, and these particles will produce defects at the impact point. The binding energy of these defect areas on the surface of the substrate is higher than that of the adjacent areas, so they preferentially become nucleation points, which is conducive to the accelerated growth of the film, the increase of the deposition amount of the film, and the increase of the thickness of the film.

However, it is not that the higher the sputtering power, the more favorable the film deposition is. If the sputtering power is too high, the kinetic energy of the sputtering ions will be significantly increased. If the ion energy is too high, the substrate heating effect will be more significant, the film will be damaged, and the quality of the film will be reduced. Xiong et al. used the non-equilibrium magnetron sputtering technique to deposit CN thin films on Si wafers[64] and found that with the increase of sputtering power, the deposition rate decreased instead, as shown in figure 14. This is because when the sputtering power is significant, the ionized ions have high energy, the depth of the ions into the target material increases, and the energy loss increases, which escapes the sputtered atoms more complex, and the target atoms are not easy to escape，reducing the deposition rate. At the same time, due to the increase of sputtering power, the secondary electrons generated during sputtering increase, which will have a particular heating effect on the substrate, volatilize the CN groups deposited on the substrate and reduce the deposition rate.
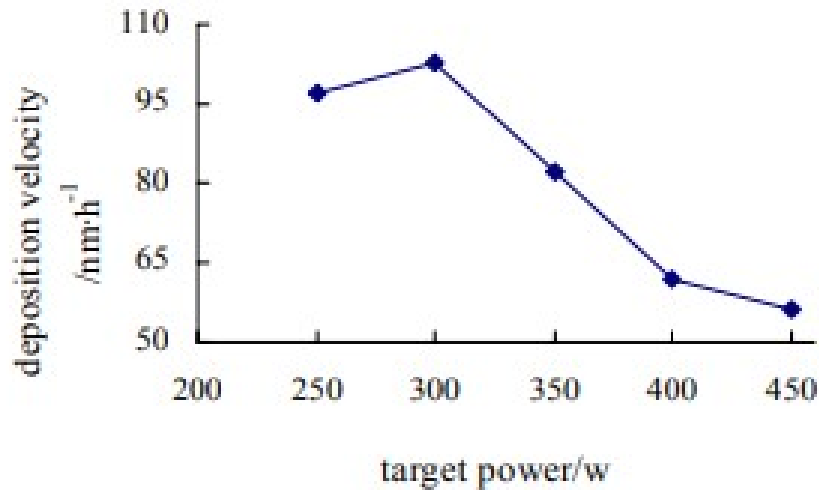
Figure 14. Influence of target power on deposition rate.

Gao et al. used RF reactive magnetron sputtering to prepare chromium oxide films on No. 45 steel [65]. They obtained the curves of deposition rate and film grain size as a function of sputtering power while keeping the oxygen flow rate unchanged, as shown in Figure 15. With the increase of sputtering power, the deposition rate increases, and the grain size first decreases and then increases slowly.

According to the research of Yamamura [66] , and according to the surface binding energy of each target atom, the threshold voltage of different target materials can be calculated when argon ions are incident ions, the sputtering threshold for sputtering Ti targets, Cr targets, and Cu targets (when the energy of the incident ions is more significant than a specific value, only the atoms of the target material are sputtered, and the atoms are sputtered out. The critical values are called sputtering thresholds) are 20eV, 22eV, and 17eV, respectively. The energy of the incident ions is proportional to the sputtering power, and the sputtering power directly adjusts the energy of the incident ions. The sputtering yield is related to the atomic mass of the target and the composition of the target. Different atomic masses of the target lead to different sputtering thresholds and different sputtering yields. For a target with a

small sputtering threshold, under the same sputtering power, the obtained sputtering yield is large, and the deposition rate is high; the sputtering yield is also related to the crystallinity of the target, but the sputtering power is to control the main deposition factor in speed.

Different sputtering methods are used to deposit different films, and the influence trend and magnitude of sputtering power are also different. Considering the influence of sputtering power, the appropriate sputtering power should be found according to specific conditions.
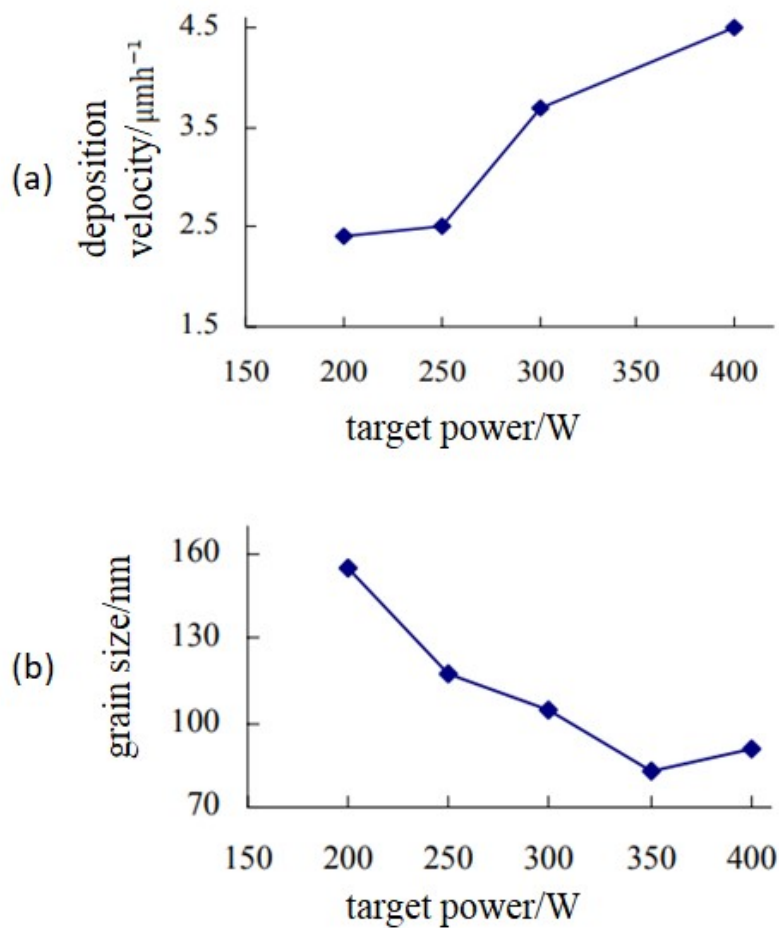
Figure 15. (a) Deposition rate of chromium oxide coatings deposited at an O_2 flow rate of $0.8 cm^3/min$ and different RF powers (b) Grain sizes in chromium oxide coatings deposited at an O_2 flow rate of $0.8 cm^3/min$ and different RF powers.

2.3.3 Influence of target-substrate distance on electrolyte film

The sputtering pressure was set to 10mTorr, the sputtering power was 50 W, the GDC electrolyte film was sputtered and deposited, the deposition time was 4 h, and the distances from the target to the substrate were 28 cm and 30 cm, respectively. The effect of the distance from the target to the substrate on the electrolyte film was observed experimentally. The cross-section and surface results of SEM observation are shown in Figures 16 and 17.
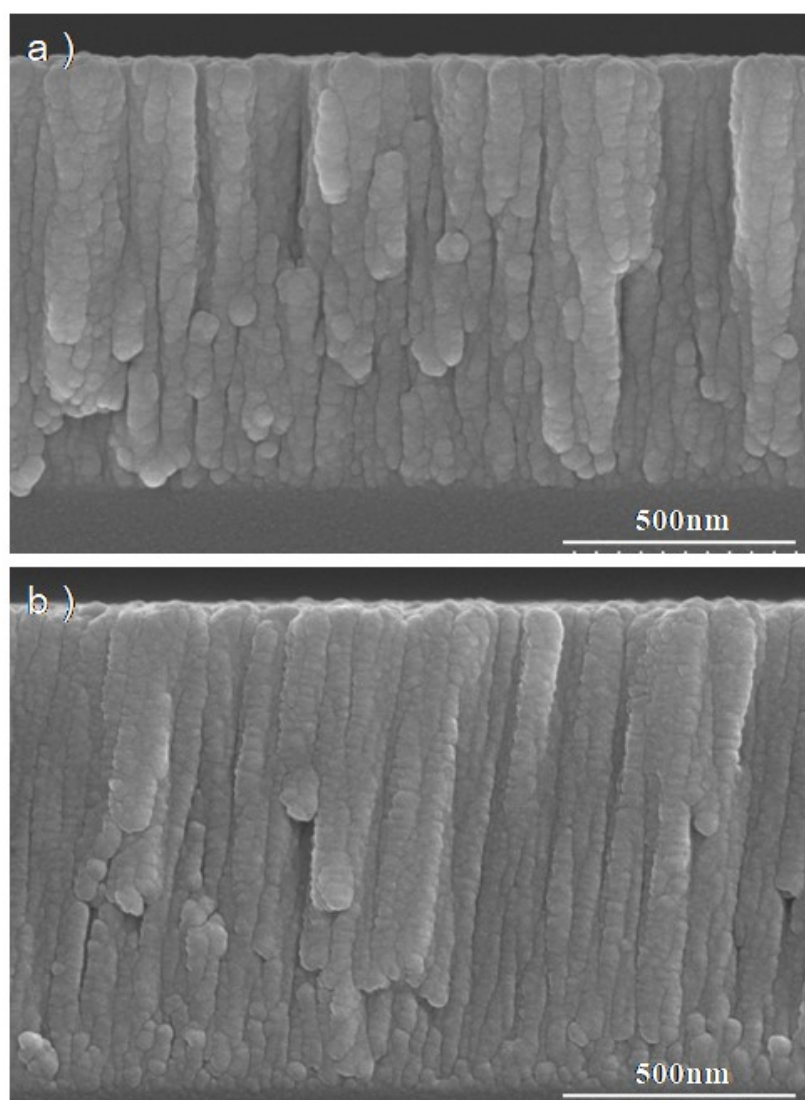
Figure 16. (a) 28cm (b) 30cm target-to-substrate distance from the SEM cross-section of the sputtered GDC electrolyte.

It can be seen from the cross-sectional view that as the distance from the target to the substrate increases, the growth of the crystal grains is better. When sputtering at 28 cm, the thickness of the resulting film is 946 nm, and the growth of the crystal grains is not orderly. As a result, the area will show a blocky distribution with poor uniformity. On the contrary, when sputtering at 30cm, the film thickness is 1.10μm, showing a relatively uniform grain arrangement. The surface map sputtered at 28 cm shows that the crystals are irregularly agglomerated and clumped without uniformity. In contrast, the surface map sputtered at 30 cm shows a more uniform and neat crystal arrangement.
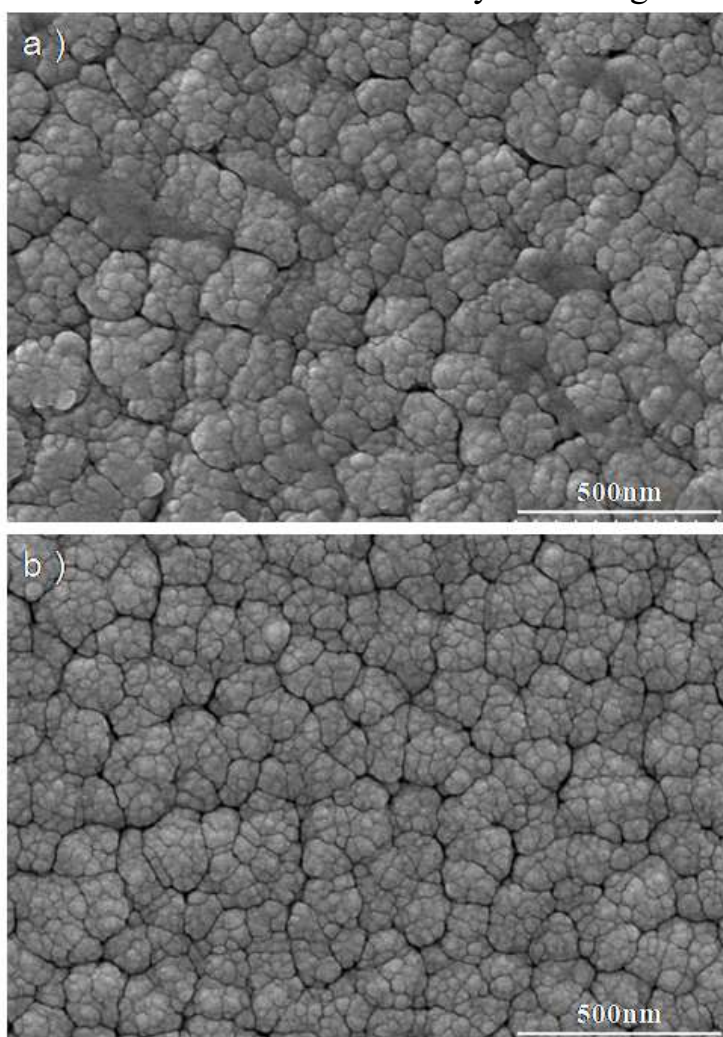
Figure 17. (a) 28cm (b) 30cm target-to-substrate surface from the SEM cross-section of the sputtered GDC electrolyte.

The relationship between the mean free path of sputtered particles and the gas concentration can be approximated as:

$$\bar{\lambda}=[\sqrt{1+\frac{m}{40}}\pi(R+R_{Ar})^2 n_{Ar}]^{-1} \qquad (3)$$

where $\bar{\lambda}$ is the mean free path of the sputtered particles, n_{Ar} is the molecular density of Ar, m is the atomic weight of the sputtered particles, R、 R_{Ar} are the atomic radii of the sputtered particles and Ar, respectively. It can be seen from the above formula that when the sputtering gas pressure is constant, the mean free path of the sputtered particles is constant. Suppose the distance from the target to the substrate gradually increases. In that case, the number of collisions with the gas ions when the sputtered particles fly towards the substrate will increase, and the probability of reaching the substrate will also decrease. At the same time, since the sputtered atoms are distributed according to cosine, as the distance from the target to the substrate increases, the probability of the substrate accepting atoms decreases, so the deposition rate decreases. The film deposition rate increases as the target-to-substrate distance decrease, but the film uniformity decreases. If the target-base distance is too small, most of the sputtered atoms will reach the substrate surface without colliding with the background gas molecules. The bombardment of the film growth surface by high-energy particles may damage the film and cause defects. If the distance from the target to the substrate is significant, the energy of the high-energy sputtering atoms will be reduced due to collisional heating. At this time, the bombardment of the film will increase the activity of the deposited particles, improve particle mobility, and help the growth of the film.

There are many studies on the influence of the distance from the target to the substrate on the deposition rate. It is pointed out by the

literature [67] that under the condition of constant sputtering power, when the distance from the target to the substrate is small, the deposition rate is usually distributed along the radial direction. Which seriously affects the deposition uniformity. When the distance from the target to the substrate increases, the uniformity increases, but when the distance from the target to the substrate continues to increase, although the uniformity is more substantial, the deposition rate decreases significantly. This is because when the distance between the target and the substrate is short, the plasma density in the coating area is high, the effect of gas scattering is small, and the film deposition rate is high. With the increase of the target-to-substrate distance, the number of collisions with gas molecules increases when the sputtered material shoots toward the substrate. The plasma density decreases, and the kinetic energy decreases, so the film deposition rate decreases.

2.3.4 The effect of other factors on the film

In addition to the main influencing factors of sputtering pressure, sputtering power, and target-to-substrate distance, there are still many factors that affect the structural properties of the film, such as vacuum chamber cleanliness, background vacuum, substrate temperature, target purity, and sputtering gas purity and many other factors. Usually, the cleanliness of the vacuum chamber and the background vacuum are the easiest to ensure.

As a special-purpose material, the target has a vital application purpose and a transparent application background. Therefore, it is meaningless to study the performance of the target material itself apart from the sputtering process and film properties. However, according to the performance requirements of the film, studying the composition, structure, preparation process, and performance of the target material, as well as the relationship between the composition, structure, performance of the target material, and the performance of the sputtered film, is beneficial to obtain the film performance that meets the application needs. It is also conducive to better use of the target material, gives full play to its role, and promotes the development of thin-film technology applications.

The purity of the target material has a significant influence on the performance of the sputtered film. The higher the purity of the target material, the better the uniformity of the sputtered film, the fewer surface defects, and the better the film performance. The purity of commonly used metal targets is shown in Table 2. At the same time, the purity of the sputtering gas also has a particular influence. Taking the commonly used argon gas as an example, when the Ar ions hit the target surface during the sputtering process, some of them are mixed

into the sputtered target atoms and deposited on the surface of the substrate. Therefore, if the purity of argon gas is not enough or too many impurities are mixed in during sputtering, many defects will be formed in the film layer. After sputtering a film of a certain thickness, the film layer will be loose, which will have a significant impact.

According to the analysis of the substrate's surface temperature, increasing the substrate's temperature is conducive to the mutual diffusion of the film and the substrate atoms. It will accelerate the chemical reaction, which is conducive to the formation of diffusion bonding and chemical bond adhesion, which increases the adhesion. However, suppose the substrate temperature is too high. In that case, the grains of the film will be coarse, the thermal stress in the film will increase, and the tendency of film cracking and peeling will increase, thereby reducing the quality and performance of the film. Therefore, it is necessary to comprehensively consider the influence of the substrate temperature and select the appropriate substrate temperature for different films or substrates to obtain films with better adhesion properties.

Metal	Purity/%	Metal	Purity/%
Al	99.99	Pb	99.99
Cr	99.98	Bi	99.95
Co	99.90	Sb	99.90
Cu	99.99	Zn	99.99
Au	99.99	Ni	99.90
Ag	99.99	Mn	99.95
Pt	99.95	Nb	99.90
Pd	99.90	W	99.90
Hf	99.90	Ta	99.95
In	99.99	Ti	99.50
Fe	99.90	Zr	99.90
Sn	99.99	V	99.90

Table 2. Purities of a few metal target materials.

2.4 Conclusion

Through the above experiments and analysis, we can find that as the sputtering pressure increases, the crystallization of the film is better, and the grains grow in the vertical direction under high sputtering pressure, showing a neat columnar grain arrangement. The film thickness Increase first and then decrease. The increase of sputtering

power will increase the ionization degree of the discharge carrier, increase the density of the ions, increase the sputtering rate, and make the sputtered ions have higher energy, thereby improving the adhesion of the film or the substrate and the adhesion of the film. Density the film thickness increases. As the distance from the target to the substrate increases, the film shows better uniformity. The high-energy sputtering atoms are thermalized due to collision, decreasing the energy. At this time, the bombardment of the film will increase the activity of the deposited particles and improve Particle mobility, contributing to thin-film growth. Many other factors will affect the film more or less, so selecting the appropriate process conditions for sputtering the film correctly is necessary.

From the cross-section and surface images of 3 YSZ, it can be seen that the typical columnar structure is not apparent, and there are no irregularly shaped protruding islands in the surface image. It is because the sputtering pressure is low, the gas is less, the mean free path of the sputtered atoms is longer, and the atoms have more energy to grow preferentially, so the grains of 3YSZ are denser.

The adhesion between the film and the substrate is a key factor restricting the use of magnetron sputtering films. Improving the surface state of the substrate, optimizing the process parameters, and reasonably matching the film or the substrate are all effective ways to obtain a film with better adhesion properties. Providing compositionally or structurally graded transition layers is also an effective way to improve film or substrate adhesion and mechanical properties. In the actual coating process, according to the specific matching substrate or film, the appropriate process conditions are found through experiments, and a film with better quality is obtained.

CHAPTER3. XRD and Residual stress

3.1 Introduction

3.1.1 Introduction to film stress

The stress of the film is a macroscopic phenomenon. However, it reflects the internal state of the deposited film and is an essential factor determining the integrity of the entire film. When the film stress is severe, it will directly lead to film cracking, peeling off, and damage to the film surface and overall performance. The principle of sputtering coating is that the atoms generated by sputtering are deposited on the surface of the substrate to form a film, and gas discharge is used to generate gas ionization. The positive ions bombard the cathode target at high speed under the action of the electric field, bombard the atoms or molecules in the cathode target, and fly to the surface of the plating substrate to deposit into a thin film. The various mechanisms in such a physical process will inevitably cause stress effects[68], [69] , and the substrate deformation can be observed macroscopically, as shown in Figure 18.
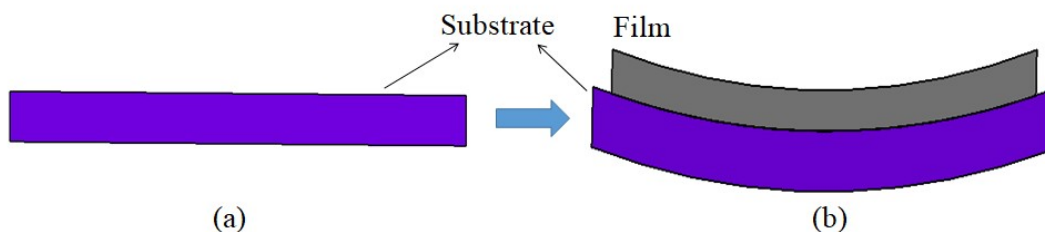
Figure 18. (a) Substrate before film formation (b) Substrate after film formation, substrate deformation due to deposition of thin films.

Films are usually supported by an attached substrate, and the substrate material affects the structure and properties of the film. Therefore, the film and the substrate form a unified whole of mutual connection and interaction. This interaction is usually manifested in the form of two forces on the macroscopic level. The first force is the adhesion of the bonding strength between the contact interface between the film and the substrate. The second force is the force (film stress) from the matrix constraint on the unit section of the reaction film. At the same time, the film stress can be divided into tensile stress and compressive stress in the acting direction[70] . The matrix exerts tensile stress on the film if the film has a tendency to shrink along the film surface, and conversely, the expansion tendency of the film along the film surface causes compressive stress[71]. We can conclude that the adhesion between the film and the substrate is a prerequisite for the generation of film stress, and the existence of film stress has an important influence on the adhesion.
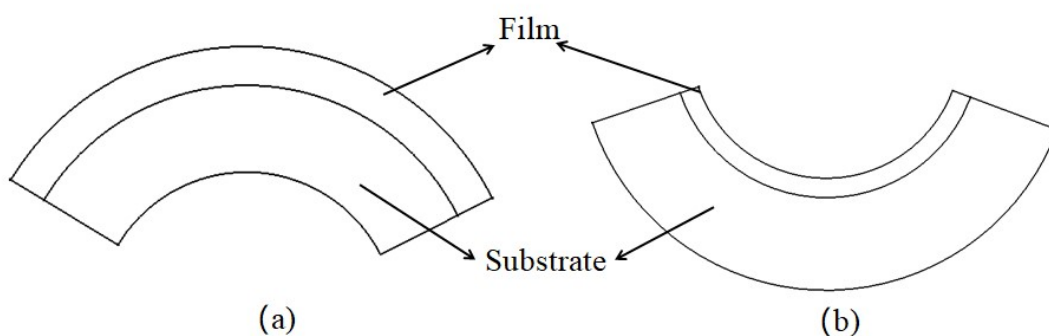
Figure 19. (a) Compressive stress (b) Tensile stress, Schematic diagram of the relationship between the two stresses.

In a brief summary, stress can be divided into three categories. The first stress category is the stress that maintains equilibrium in an extensive range of objects or a large number of grains, which is usually called macroscopic stress (residual stress). The second and third types are internal stresses that maintain equilibrium within a minimal number of grains and atoms, collectively called microscopic stresses[72]. The stress in the film is affected by many factors. The film deposition process, the heat treatment process, and the material's mechanical properties are the main influencing factors. According to the source of stress, the stress in the film is divided into thermal stress and intrinsic stress, and the commonly mentioned residual stress is the comprehensive application of these two stresses.

Thermal stress is caused by the difference in thermal expansion coefficients between the film and the substrate. During the coating process, the temperature of the film and the substrate both increase simultaneously. Therefore, after the coating, when the temperature drops to the initial temperature, internal stress is generated due to the different thermal expansion coefficients of the film and the substrate, generally called thermal stress. This phenomenon is called the bimetallic effect[73]. However, thermal stress caused by this effect cannot be considered an assertion. The film thermal stress refers to the internal stress of the film due to the thermal expansion and contraction effect of the constrained film under the condition of changing temperature. Intrinsic stress, also known as internal stress, is generated in the film deposition growth environment (temperature, pressure, gas flow rate) because its formation causes are complex. There is no systematic theory to explain it, such as lattice loss. Internal stress will be generated due to coordination, impurity intervention, lattice reconstruction, and phase transition[74]. The thermal stress is mainly

caused by the difference in thermal expansion coefficient between the film and the substrate, which can be expressed as:

$$\sigma_T = \int_{T_m}^{T_s} E_f \left(\alpha_f - \alpha_s\right) dT \qquad (4)$$

where d is the thickness of the film, E_f where d is the thickness of the film, α_f and α_s are the thermal expansion coefficients of the film and the substrate, respectively, T_m is the room temperature, T_s is the substrate temperature during film deposition, and σ_T is the thermal stress.

Intrinsic stress can be further divided into interface stress and growth stress. The interface stress originates from the lattice dislocation or high defect density between the film and the substrate at the contact interface. In contrast, growth stress is closely related to the movement of various structural defects during the film growth process. The intrinsic stress is closely related to the preparation method and process of the thin film and varies with the difference between the thin film and the matrix material. Furthermore, the intrinsic stress of the film is related to the microstructure and defects of the film, so the interaction between grain boundaries and boundaries has been paid attention to it. By choosing different film materials, different coating methods, and different deposition processes, the magnitude and nature of the internal stress in the film can be changed, which is also a key content of this paper.

Many laboratories and thin-film researchers worldwide have researched the causes of thin-film stress and have proposed various theoretical models. However, the stress phenomenon is very complex, and it is closely related to the raw materials and the process parameters of the deposition process. Therefore, each combination of materials and deposition processes needs to be carefully studied. At present, the

following models are proposed for the causes of stress:

（1）Model of heat shrinkage effects

Wilman and Murbach proposed a model of stress generated by thermal shrinkage[75] , which is based on the premise that the temperature of the uppermost layer of the film will reach a relatively high temperature during evaporative deposition. The evaporated meteorological atoms deposited on the substrate have high kinetic energy during the film formation process. When the deposition process is over and the film is cooled to room temperature, the atoms inside the film gradually show an immobile state (with the recrystallization temperature as the critical standard) and thermal shrinkage below the recrystallization temperature is the cause of stress.

（2）Phase transfer effect model

A gas phase to solid phase transition occurs during film formation. In phase transition, volume changes are usually caused, resulting in stress.

（3）Lattice defect removal model

Lattice defects exist in the film after thermal annealing. These defects are eliminated when atoms diffuse on the surface, and the volume shrinks to form internal stress of tensile stress nature.

（4）Interface mismatch model

When a thin film material with a significant difference in lattice structure from the matrix forms a thin film on the matrix, if there is a strong interaction between the two, the lattice structure of the formed thin film will be similar to that of the matrix, so the thin film Internal stress is formed due to the internal distortion.

（5）Impurity effect model

The ambient atmosphere contains a large amount of oxygen, water

vapor, nitrogen, and other gases. During the film formation process, impurities in the ambient atmosphere will cause changes in the film's structure. Impurity gas atoms adsorb or remain in the film to form interstitial atoms, resulting in lattice distortion. Even chemical reactions such as diffusion, migration, and boundary oxidation may occur inside the film. The more residual gas penetrates the film as an impurity, the easier it is to form a more considerable compressive stress. In addition, due to the diffusion between grain boundaries, impurity diffusion will also occur at low temperatures to form compressive stress.

（6）Atomic and ion pinning effect model

In the process of film sputtering deposition, the most notable feature is that there are working gas atoms, and the energy of the sputtering atoms is relatively high. Under lower working gas pressure, a film in a state of compressive stress is usually obtained. The conclusion has great generality[76]. In this regard, Hoffman and Thormon et al. proposed the atomic pinning effect model[77].

（7）Improved TFD (Thomas-Fermi-Dirac) theory

The TFD theory generally believes that the difference in the surface electron density of the film material and the substrate material is the cause of internal stress. Therefore, at the interface between the film and the substrate, the surface electron density must remain continuous. This theory reveals some ways to control and reduce the internal stress of the thin film. Selecting the corresponding suitable materials in terms of material selection, dimension design, and process technology is beneficial to reducing the internal stress in the thin film. Now, researchers have adjusted the surface electron density of the material by ion implantation, which can significantly reduce the residual stress in the film[78], [79].

The above theoretical models show that the origin of film stress involves complex physical and chemical processes, which are closely related to the nucleation, growth process, and microstructure of the film. In general, the generation of stress results from the combined action of several mechanisms.

3.1.2 Measurement method of film stress

Residual stress is usually generated during the deposition and growth of thin films. Residual stress in thin films is one of the fundamental reasons for the failure of thin films and related devices. Excessive residual stress may lead to delamination, buckling, and microcracks. Moreover, stress can also cause other problems, such as weakening the bonding strength of the film, producing crystal defects, destroying the integrity of the epitaxially grown film, and producing abnormal precipitation on the film's surface, affecting the hysteresis loop and butterfly curve of the ferroelectric film [80]–[82].

There are many coating methods, but the generation of residual stress in the film is inevitable, whether using chemical vapor deposition, physical vapor deposition or magnetron sputtering, or other coating techniques. During the manufacturing process, the workpiece will be affected by various factors such as processes. When these factors disappear, if the effects mentioned above and influences on the components cannot be eliminated, and some of the effects and influences remain in the components, the residual effects and influences are also called residual stress. No matter which coating method is used, when the film material is vapor-deposited on the substrate in a vacuum chamber, this phase transition will cause a significant change in the volume of the film material due to the change from gas to solid. This

change plus the deposition The extrusion or stretching of atoms (or molecules) and atoms (or molecules) will cause internal stress due to micropores and defects during the film formation process. Therefore, it is necessary to study the residual stress value.

In the study of film stress, only macroscopic stress is generally considered, usually based on strain measurement, and then calculated according to elastic theory. Now the measurement methods of film stress include substrate curvature method[83] , X-ray diffraction method (XRD) , neutron diffraction[84] , optical interferometry[85] and Raman spectroscopy[86] . The substrate curvature method calculates the film stress by measuring the curvature change of the substrate before and after coating. When the thin film is deposited on the substrate, two-dimensional interfacial tension is generated between the thin film and the substrate, causing the substrate to bend slightly. The correspondence between the substrate curvature change and the film stress can be deduced from geometrical and mechanical principles, which can be expressed by the Stoney formula[87], [88]:

$$\sigma = \frac{E_s t_s^2}{6(1-\eta_s)d_f}\left(\frac{1}{R} - \frac{1}{R_0}\right) \qquad (5)$$

where R_0 and R are the radii of curvature of the substrate before and after coating, t_s ,E_s,and η_s are the thickness, Young′s modulus, and Poisson′s ratio of the substrate, respectively, and d_f is the film thickness. However, due to the two-dimensional interfacial tension between the film and the substrate, the substrate is slightly bent, which means that the substrate is damaged to varying degrees, which we do not want to see.
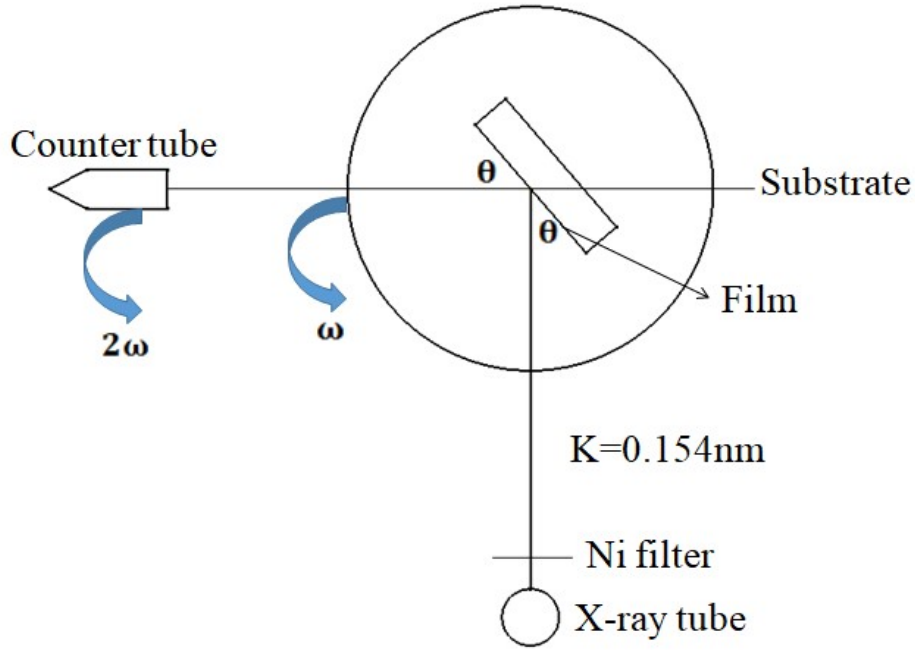
Figure 20. X-ray Diffraction Apparatus

The method used in this experiment is the X-ray diffraction method, which is a standard method for stress measurement of semiconductor thin films and crystal thin films. Under the action of stress, the lattice will be distorted so that the lattice constant will change, so the measured lattice distortion can be calculated, and the stress of the film. The X-ray diffraction method is shown in Figure 20. The sample is placed on the goniometer, and the distance between the atomic planes of the film can be obtained according to the Bragg angle θ of the diffraction peak:

$$2d\sin\theta = \lambda \ (\lambda=0.15405nm) \tag{6}$$

assuming that the interplanar atomic spacing of the bulk material when the crystal is not distorted is d_0, the internal stress of the film is:

$$\delta = \frac{E_f}{2\eta_f} \frac{d_0 - d}{d_0} \tag{7}$$

where d_0 and d are the interplanar atomic distances when no distortion occurs and when distortion occurs, respectively, and E_f and

η_f are Young's modulus and Poisson's ratio of the thin film.

X-ray diffraction measurement has many advantages. For example, there is no need for unstressed standard samples; it is possible to measure film stress macroscopically or microscopically; the measurement process is not destructive, and the measurement accuracy is high[89] . However, at the same time, there is also a requirement that the thin film is a single crystal or polycrystalline material, and it is impossible to directly measure the stress of the amorphous structure thin film commonly used in the device process.

Recently, many new methods have appeared to measure residual stress. For example, Ma et al. used the grazing incidence method to measure residual stress[90] . Inhomogeneous specimens have little effect on residual stress results. E. Bemporad studied the FIB-DIC technique to analyze residual stress depth gradient is possible[89].

X-ray diffraction is a non-destructive testing method and is the most commonly used method for testing residual stress in brittle and opaque materials. In 1961, E. Mchearauch of Germany proposed the $\sin^2\psi$ method of X-ray stress measurement, which made a big step forward in the practical application of stress measurement[91], [92].The principle is that when there is residual stress on the surface of the isotropic material, since the X-ray penetration depth is very shallow (generally only tens of microns for traditional materials), it can be considered that the material's surface is in a state of plane stress. At this time, different azimuth angles ψ The X-ray diffraction peaks of the diffracting crystal planes are shifted accordingly; the (HKL) interplanar spacing d_{hkl} has a linear relationship with $\sin^2\psi$. At this time, the $d_{hkl}\sim\sin^2\psi$ curve can be fitted to obtain the residual stress in the material. The basic formula for measuring residual stress by the $\sin^2\psi$ method is:

$$\frac{d-d_0}{d_0} = \frac{1+\nu}{E}\sigma\sin^2\psi - \frac{2\nu}{E}\sigma \tag{8}$$

where E and ν are the elastic modulus and Poisson's ratio, and d and d_0 are the interplanar spacings corresponding to the diffraction planes of the stressed and unstressed samples. Considering the small scale of thin films in the expected direction, this method applied in bulk materials was successfully transplanted to residual stress measurement of thin films. However, for films with sizeable average thickness and no firm texture, the stress measurement based on the traditional $\sin^2\psi$ method can also achieve ideal results. Using the measured diffraction line displacement as the raw data, the measured result is the residual strain, and the residual stress is calculated from the residual strain by Hooke's law. When there is residual stress in the sample, the interplanar spacing will change, and when Bragg diffraction occurs, the resulting diffraction peak will also move, and the moving distance is related to the size of the stress.

By understanding the source of residual stress, take specific measures to eliminate or significantly reduce the residual stress inside the membrane mechanism and avoid various failure forms caused by residual stress. Through real-time monitoring and control of residual stress during the process, process parameters can be improved, and unstable factors can be eliminated or controlled. We usually use thermal annealing, add sub-thin film layers to control multilayer film stress, or change process parameters and deposition technology to control residual stress. For example, David et al. studied the residual stress in sputter-deposited YSZ films due to deposition pressure and substrate temperature[93] . They found that the intrinsic stress level can vary from about 500 Mpa in compression to 50 Mpa in tension, with thickness and processing parameters changing. Furthermore, the

temperature cycling of the deposited films showed up to a 400Mpa change in the film's intrinsic stress state, resulting in a final room temperature stress level of the film reaching a tensile strength of 250Mpa. These data are used to design and fabricate thermomechanically stable membrane structures for microfabricated solid oxide fuel cells. In this experiment, XRD was used to measure and calculate residual stress. In addition, a scanning electron microscope (SEM) was used to observe the cross-section and surface morphology of the film to analyze the effect of residual stress on the film.

3.2 Result & Discussion

For YSZ films prepared under different sputtering pressures (3 mTorr, 5 mTorr, 10 mTorr, 20 mTorr), each film's crystallinity and residual stress were studied by XRD, and the results are shown in figure 21. The XRD patterns of each film have peaks at the same position, corresponding to the cubic phase YSZ.
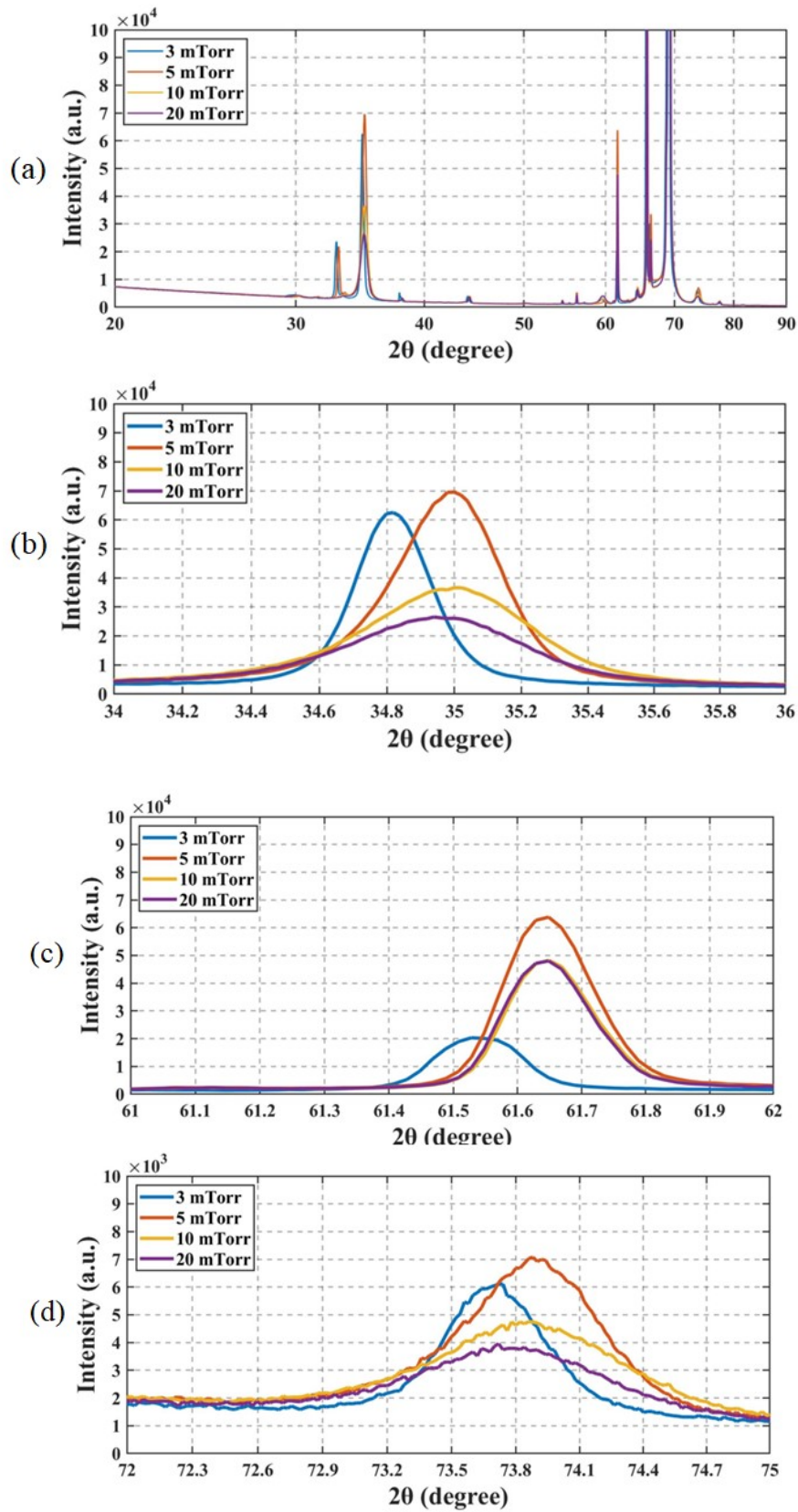
Figure 21. X-ray diffraction for investigation of crystallinity and residual stress of each electrolyte (3,5,10,20 YSZ).

Image 21(a) shows the XRD patterns of thin films prepared under four sputtering pressures. However, because the drawn XRD patterns have a high degree of coincidence and some peaks fluctuate wildly, it is difficult to observe the XRD patterns under different sputtering pressures precisely. Therefore, three parts with characteristic peaks at 34-36 degrees, 61-62 degrees, and 72-73 degrees are selected to be plotted separately, namely the three parts (b), (c), and (d) in Figure 21.

It can be seen from the enlarged XRD pattern that with the increase of sputtering pressure, the angle of the peak increases, which indicates that the stress on the film changes from compressive stress to tensile stress. The 5mTorr, 10mTorr, and 20mTorr sputtering pressures all show an increase in the peak to high angles, which is a manifestation of tensile stress, and only 3mTorr sputtering pressure shows compressive stress. When the film is prepared by sputtering, compressive stress is often generated. This compressive stress is generally the inherent stress in the sputtered film. During the sputtering process, the sputtered atoms incident on the cell membrane has energy of about 10eV. The energy is about 1 to 2 orders of magnitude higher than that of vacuum evaporation, so interstitial atoms may be formed during film formation to increase the volume of the film. In addition, accelerated particles or accelerated neutral atoms in the sputtering process often impact the film with an energy of about $10^2 \sim 10^4$eV . In addition to being accidentally captured by the film as impurities, atoms on the film's surface also The volume of the film increases due to internal movement and embedding, and compressive stress is formed in the film. The existence of compressive stress makes the grains grow in a dense direction. In addition, due to the diffusion effect between grain boundaries, impurity diffusion can occur even at low temperatures to form compressive stress. During film deposition, large and small

vacancies are formed. These vacancies will cause tensile stress, and the tensile stress will cause the grains to grow vertically upward. During the growth process, pores are generated.

Changes in process parameters during coating directly affect the final residual stress level in the film by adjusting the process parameters such as substrate temperature, sputtering pressure, and deposition rate. During coating, the magnitude of the stress in the film can be controlled, and even the nature of the force can be changed[94]. For sputtered thin films, with the increase of sputtering pressure in the reaction chamber, the concentration of high-energy ions (particles) increases, which reduces the free path of gas molecules, and there is a scattering phenomenon of serious collisions with each other, thereby reducing the gas molecules. The effect of energy and atomic shot peening is weakened, increasing the oblique component of the deposited particle flow, resulting in a loose film structure. The compressive stress becomes smaller and smaller and then becomes the tensile stress. The value of the tensile stress first increases and then decreases. This change The law is quite general in sputtered thin films[95]. This is consistent with what we observed in the figure; the tensile stress decreases as the sputtering pressure increases and reaches a meager value when the sputtering pressure increases to 20mTorr.

Considering parallel crystal planes with spacing d, the incident radiation lies in the plane of the paper. The difference in the travel of rays reflected from adjacent parallel crystal planes is $2d\sin\theta$, which is measured from the mirror surface. When the travel difference is an integer multiple of the wavelength, the radiation from successive planes will interfere constructively, which is Bragg's law [96], [97]. According to Bragg's law, the lattice distance can be calculated. When the lattice distance d is larger than the normal phase, it indicates residual stress in

the plane direction of the film.

$$\text{Bragg's law: } 2d\sin\theta = n\lambda \qquad (9)$$

where d is the distance between parallel atomic planes, λ is the wavelength of the incident wave, and θ is the angle between the incident light and the crystal plane. After we have obtained the distance d between the planes of the parallel atoms, the value of the residual stress can be calculated.

$$\sigma_\phi = \frac{E}{(1+\nu)d_0}\left(\frac{\partial d_\psi}{\partial \sin^2\psi}\right) \qquad (10)$$

where E is Young's modulus, ν is Poisson's ratio, and d_0 and d_ψ are lattice spacing without stress and lattice spacing with stress. Because when the sputtering pressure is 20mTorr, the residual stress value between films tends to zero, calculate the residual stress under the sputtering pressure of 3mTorr in the characteristic peaks (b), (c), and (d) in Figure 21, are 169.983Mpa, 160.292Mpa, and 154.960Mpa. The residual stress values under 5mTorr sputtering pressure are 169.018Mpa, 160.031Mpa, and 154.666Mpa. In contrast, 3mTorr shows higher residual stress values and a high extrusion between grains. The pressed state further confirms the high density of the film at 3mTorr.

As the sputtering pressure increases, the film shows better crystallinity. During the grain growth process of the film, when the sputtering pressure is low, the grains grow laterally, and adjacent grains collide with each other during the growth process. Extrusion produces residual stress. It can be seen from the cross-sectional view of the thin film prepared under the sputtering pressure of 3mTorr that the typical columnar structure is not apparent. The less gas is present, the longer the mean free path of the sputtered atoms. Atoms have more energy to

grow preferentially. On the contrary, for the YSZ film prepared under the 10mTorr and 20mTorr, due to its higher sputtering pressure, the probability of collision and scattering of atoms sputtered from the target increases before reaching the substrate, and the energy of the sputtered atoms decreases. The migration ability after the substrate decreases. During the film formation process, the nucleus's density increases, the nucleus's size decreases, and the size of the resulting grains decreases. The grains do not contact each other and grow vertically upward, and residual stress is minimal or non-existent.

However, the problem also arises because the grains grow preferentially in the vertical direction under the higher sputtering pressure, and the grains do not interfere with each other, showing a neat columnar arrangement. The appearance of neat columnar grains that are not in contact means that the generation of pores in the YSZ film will have a severe impact. As we all know, the solid oxide fuel cell is a new power generation device with an all-solid structure and wide adaptability to various fuel gases. The anode side of the solid oxide fuel cell is continuously fed with fuel gas, such as hydrogen（H_2）, methane （CH_4）, or city gas, the catalytic anode surface adsorbs the fuel gas and diffuses to the interface between the anode and the electrolyte through the porous structure of the anode, and oxygen or air is continuously introduced on the cathode side. When the film has pores under high sputtering pressure, when the fuel gas (take hydrogen as an example) passed into the Ni anode passes through the pores existing in the electrolyte film and reaches the Pt cathode through the electrolyte film, it means that hydrogen leaks, the leakage of hydrogen will cause the performance of the fuel cell to decline. At the same time, hydrogen is a flammable gas. Too much accumulation will bring about a more significant safety hazard. In severe cases, an explosion will occur,

which is something we do not want to see.

At the same time, hydrogen, the lightest element, leaks from pores more easily than liquid fuels and other gaseous fuels. If a leak occurs, the hydrogen will diffuse rapidly. Compared with gasoline, propane, and natural gas, hydrogen has greater buoyancy (rapid rise) and greater diffusivity (lateral movement). In addition, hydrogen has a wide combustion range and a shallow ignition point in the air. The hydrogen flame is almost invisible to the naked eye because, in the visible light range, the burning hydrogen emits very little energy, which significantly increases the danger.
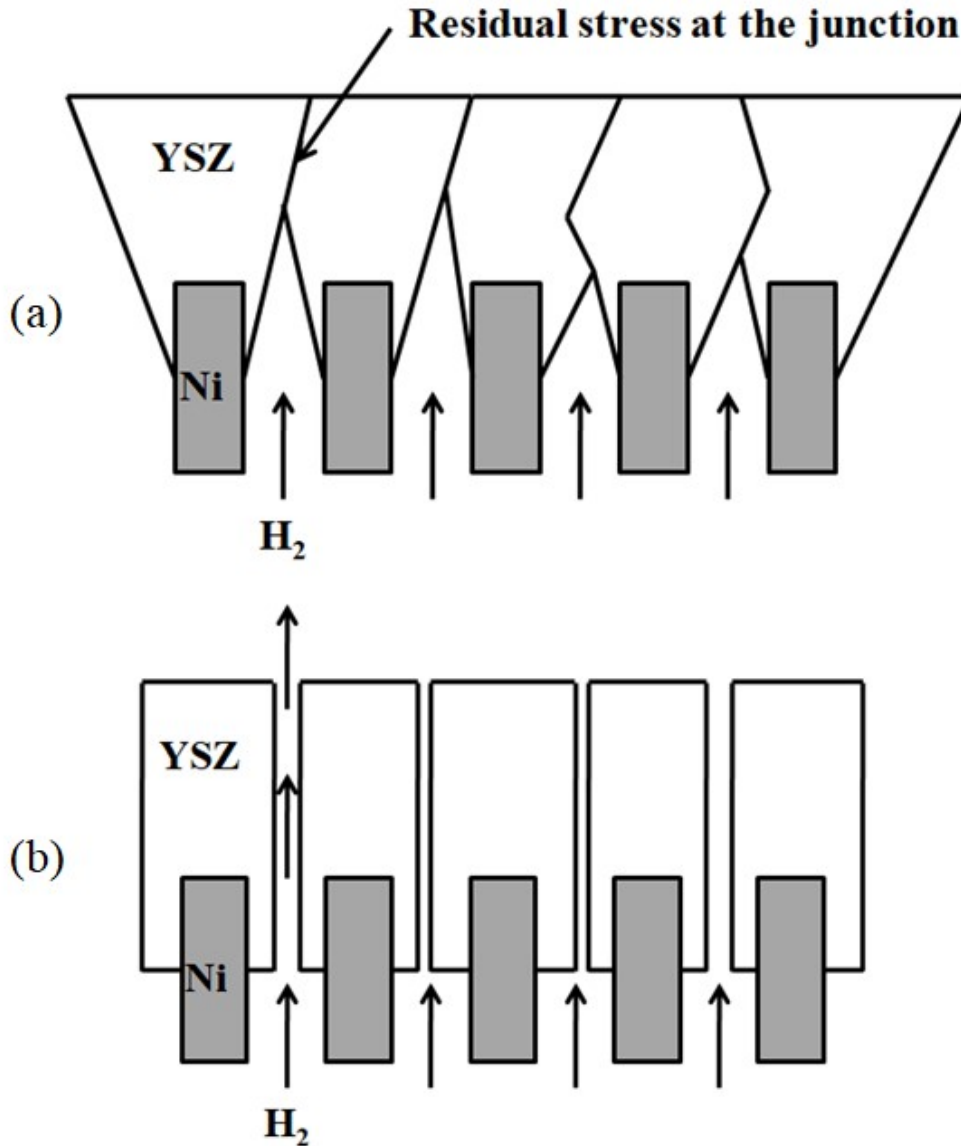
Figure 22. (a) 3mTorr (b) 5,10,20mTorr，YSZ film growth condition.

The research on hydrogen leakage and diffusion mainly includes experimental research and numerical simulation[98], [99] . However, due to the high risks associated with hydrogen and the high cost of conducting related experiments, experimental studies on hydrogen leak-diffusion are rare, and numerical simulation is still the mainstream method currently used to study hydrogen leak-diffusion processes. In conclusion, it is not advisable to use microporous films prepared under high sputtering pressures as electrolyte films for solid oxide fuel cells.

3.3 Conclusion

The XRD method investigated the crystallinity and residual stress of the films prepared under different sputtering pressures. We can see from the XRD patterns that with the increase of sputtering pressure, the angle of the peak increases, and the crystallinity of the grains increases. The better the degree of sputtering, the average grain size of the YSZ film decreases with increasing pressure.

The increase in the diffraction peak angle in the XRD pattern indicates that the stress state on the film is transformed from a compressive state to a tensile state. When the sputtering pressure is 3 mTorr, the stress state appears as compressive stress, and the existence of compressive stress makes the grains grow in a dense direction. In addition, due to the diffusion effect between grain boundaries, impurity diffusion can occur even at low temperatures to form compressive stress. When the sputtering pressure reaches 5mTorr or more, the stress state is tensile stress, and large and small vacancies will be formed during film deposition. These vacancies will cause tensile stress, and the tensile stress will make the grains vertical. The upward growth produces a different number of pores during the growth process. The generation of pores will seriously affect the performance of the fuel cell, and in severe cases, an explosion will occur.

Bragg's law is used to calculate the lattice spacing. When the lattice distance is larger than the normal phase, the existence of residual stress is proved. The residual stress of the film prepared under the sputtering pressure of 3mTorr is higher than that of the film prepared under the high sputtering pressure and better density. In conclusion, the films formed by sputtering under the sputtering pressure of 3mTorr showed the best stress state.

CHAPTER4. Electrochemical evaluation of thin-film fuel cells

4.1 Fuel cell performance research

The anode side of the solid oxide fuel cell needs to be tightly sealed due to the use of fuel gas. A small leakage of fuel gas can affect the study of cell performance. Under the condition of nitrogen protection, the company seals when the temperature rises to the softening temperature of the glass, monitors the change of the open-circuit voltage during the heating process, and preliminarily checks whether the fuel cell is sealed. Then water vapor was introduced to humidify the hydrogen, and the partial pressure of oxygen on the anode side at the test temperature was calculated. The oxygen partial pressure of the air electrode was 0.21 atm, allowing the theoretical open-circuit voltage of the single cell to be calculated. When the actual measured open-circuit voltage does not change with the change of fuel gas flow and is consistent with the theory, it proves that the anode seal meets the test requirements. The most critical parameters of SOFC, such as cell open-circuit voltage (OCV), output voltage, output current density, output power density, and cell efficiency, can be obtained by measuring with electrochemical methods in electrochemical workstations.

A concept called open-circuit voltage (OCV) is introduced here, and it is necessary to characterize the electrochemical open-circuit voltage of solid oxide fuel cell materials[100], [101] . The open-circuit voltage is the potential difference between the positive and negative electrodes when no current flows. In the existing fuel cell system, the potential established at the two poles of the fuel cell is primarily stable, so the open-circuit voltage is the difference between the stable potentials of

the two poles. The main factors affecting the open-circuit voltage are the nature of the fuel cell bipolar system, the nature of the material, the composition and concentration of the solution, the temperature, and the state of the electrode boundary. If the materials of the positive and negative electrodes of the fuel cells are precisely the same, then no matter how big the fuel cell is and how the geometry changes, the open-circuit voltage will be the same.

Its formation is a primary circuit with a power supply, connecting conductors, and loads, if there is an open circuit somewhere, the voltage between the two points of disconnection is the open-circuit voltage. When the circuit is open, we can understand that an infinite resistance is connected to the open circuit. This infinite resistance is connected in series with the circuit. According to the voltage division formula of the resistance in the series circuit, the divided voltage across the infinite resistance will be the highest in a circuit, the supply voltage. Jong et al. studied the open-circuit voltage of SOFC of cerium-based thin films supported on nanoporous alumina[102] . The resulting thin films detected OCV values similar to those of bulk GDC. Matsui et al. studied the effect of SDC20-based mixed conduction on the open-circuit voltage of an intermediate-temperature SOFC in the temperature range of 723–973 K [103] . The results showed that the electronic conduction of SDC20 could be suppressed at an intermediate temperature under high humidification of fuel; this will be a helpful guide for utilizing doped cerium as an electrolyte in mid-temperature SOFCs.

4.2 Electrochemical Impedance Spectroscopy to measure conductivity

The AC impedance method means that the current (or the potential of the system) of the electrochemical system changes according to the sinusoidal law with time under the condition of small amplitude. Simultaneously measure the change of the corresponding system potential (or current) or directly measure the system's AC impedance (or admittance).For a stable linear system (assuming M), such as a sinusoidal electrical signal (voltage or current) with an angular frequency of ω ,X is an excitation signal (also known as a disturbance signal) input to the system, then a corresponding sine wave electrical signal (voltage or current) Y with an angular frequency of ω is output from the system, Y is the response signal. The following formula can express the relationship between Y and X:

$$Y=G(\omega)X \tag{11}$$

If the disturbance signal X is a sine wave current signal, and Y is a sine wave voltage signal, then G is the impedance of the system M, represented by Z; if the disturbance signal X is a sine wave voltage signal, and Y is a sine wave current signal, then call G the admittance of the system M.

G(ω)

X → ■ → Y
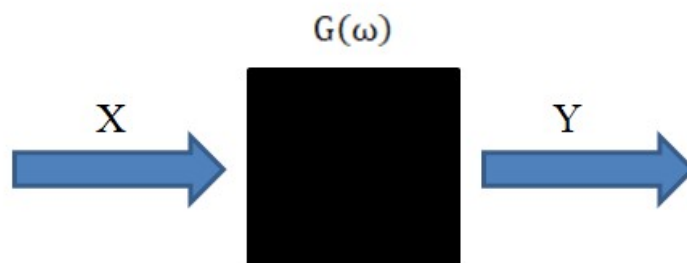
Figure 23. AC Impedance in Electrochemical Workstations

Impedance G is a vector that varies with ω, usually expressed as a complex function of angular frequency ω, namely:

$$G(\omega)=G^{'}(\omega)+jG^{''}(\omega) \tag{12}$$

where $j = \sqrt{-1}$, G' is the real part of the admittance，G'' is the imaginary part of the admittance . If G is impedance, then $Z = Z' + jZ''$, EIS technology is to measure the ratio of disturbance signal X and response signal Y at different frequencies，get the real part, imaginary part, modulus value and phase angle of impedance at different frequencies. These quantities are then plotted into various forms of curves, and the EIS reactance spectrum is obtained.

Due to the dynamic characteristics of the electrode process, the change of the electrode process velocity with the state variables generally does not obey the linear law. Only when the change of a state variable is small enough, the relationship between the change of electrode process speed and the state variable can be linearly approximated. Therefore, to satisfy the linearity condition in the impedance measurement of the electrode system, the amplitude of the sine wave point of the system or the sine wave current disturbance signal must be small so that the electrode process velocity is approximately consistent with the change of each state variable. The linear law can ensure that the response signal of the electrode system to the disturbance and the disturbance signal approximately conform to the linear condition. In general, the linear conditions of electrochemical impedance spectroscopy can only be approximately satisfied. We call the range of the amplitude of the disturbance signal when the approximate linear conditions are met as the linear range. The linear range of each electrode process is different, related to the electrode process's control parameters.

The frequency domain (frequency response) method is an engineering method to study the control system, which belongs to the most critical analysis method of the classical control theory. According to the steady-state frequency characteristic diagram of the open-loop system, the closed-loop system's stability, stability margin, and dynamic performance are analyzed. The frequency characteristic is a mathematical model of the system; there are three kinds of graphs for the frequency characteristic: amplitude-phase frequency characteristic curve (also known as polar coordinate or Nyquist curve), logarithmic frequency characteristic curve (also known as Bode diagram), logarithmic amplitude-phase frequency characteristic curve (aka Nichols curve). There is a unique correspondence between the amplitude-frequency and phase-frequency characteristics of the minimum-phase system. Therefore, the Nyquist stability criterion can be used to determine the stability of the closed-loop system from the open-loop frequency characteristics stability，and the relative stability of the system is reflected by the phase angle margin and the amplitude margin. The closed-loop frequency characteristics can be obtained from the open-loop frequency characteristics by using equal M circles and equal N circles. Then the time domain response of the system can be qualitatively or quantitatively analyzed. The characteristic of the frequency domain analysis method is that the performance (stability, stability margin, and dynamic performance) of the closed-loop system can be analyzed according to the open-loop frequency characteristics, and the influence of the system parameters on the system performance can be easily analyzed, to further improve the system—way of performance. In addition, except for some ultra-low frequency thermal systems, the frequency characteristics can be easily determined experimentally. The frequency characteristics are mainly applicable to

linear steady systems. In a linear stationary system, the frequency characteristic is independent of the amplitude and phase of the input sinusoidal signal. However, this method can also be extended to nonlinear systems under certain conditions.

Electrochemical impedance spectroscopy (EIS) is mainly used to study the relationship between AC impedance and frequency of electrochemical systems under a particular DC polarization condition, especially under the condition of equilibrium potential. From the obtained AC impedance data, the corresponding electrode reaction parameters can be calculated based on the simulated equivalent circuit of the electrodes. For example, Kawada T et al. showed that for ion-electronic mixed conductive materials, the conductivity could be accurately measured using the AC impedance method even with polarized electrodes[104] . Therefore, using the AC impedance method to measure the total conductivity is significant.

At the same time, we use the AC impedance method to measure the internal resistance of the fuel cell. The internal resistance of the fuel cell is a vital test index. The movement resistance in the fuel cell system, such as ohmic resistance (electrolyte, contact, permeation layer resistance, and transportation of reactants). However, fuel cell components include current collectors, permeation layer electrodes, catalytic layers, and contact membranes. Under external conditions such as different temperatures, pressures, humidity, and gas flow, the internal resistance of fuel cells will change to varying degrees. Impedance testing can collect various static and dynamic information about stack operations based on these changes.

4.3 Result & Discussion

To characterize the effect of electrolytes prepared under different sputtering pressure conditions, each electrolyte was applied on AAO-supported SOFCs consisting of Ni anode and Pt cathode. Electrochemical characterization was carried out at 500 °C, and the open-circuit voltage (OCV) of the electrolyte films prepared at different sputtering pressures was 1.043 V (3mTorr) and 0.735 V (5mTorr).The performance of a fuel cell can be characterized by a current-voltage characteristic diagram, that is, a current-voltage curve, which is shown explicitly as the voltage output at a given current output. At the same time, in order to make the current-voltage curves (I-V) of thin-film solid oxide fuel cells prepared under different sputtering pressures comparable, the current is usually normalized according to the effective area of the fuel cell, that is the current density (A/cm^2) is used to calculate characterization. In a fuel cell, the actual output voltage is less than the ideal thermodynamically predicted voltage. Also, the higher the output current of the actual fuel cell, the lower the voltage output, and limiting the total power that can be released. P=I×V calculates the fuel cell power. The power density curve of the fuel cell is constructed in the current-voltage curve; that is in the I-V curve, the power density curve can be obtained by multiplying the voltage value of each point by the corresponding current density value. The graphs of the curves at 3mTorr and 5mTorr are shown in Figure 24. The figure shows that the maximum power density is $1.593 \, W/cm^2$ (3mTorr) and $1.327 \, W/cm^2$ (5mTorr), respectively, and the power density decreases with the increase of sputtering pressure. Except for the electrolyte film preparation conditions, there are no other additional conditions, so the difference in power density is only due to the electrolyte change.
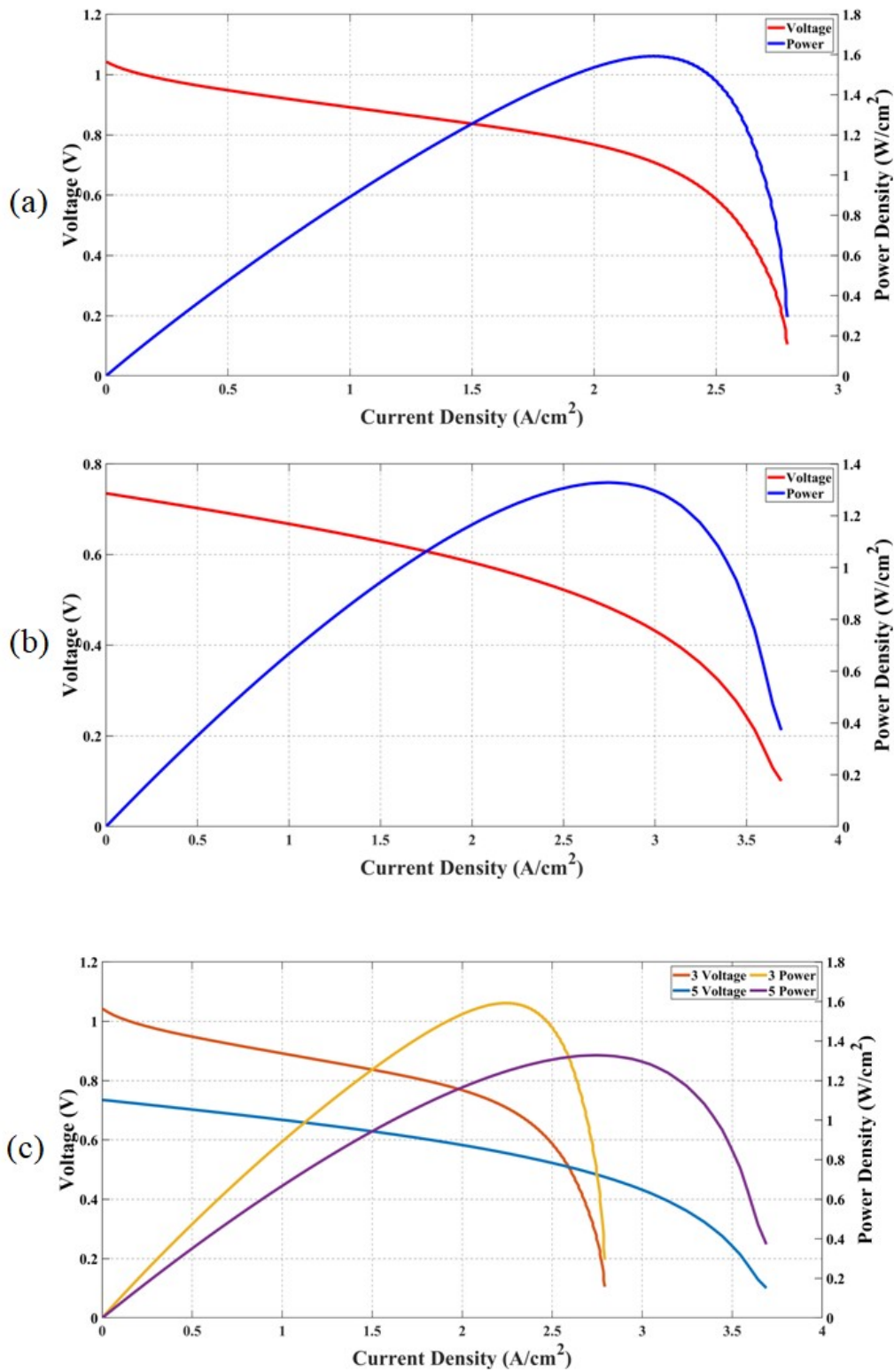
Figure 24. Voltage-Current-Power curves of AAO based TF-SOFCs with (a) 3mTorr and (b) 5mTorr (c) Overall image of 3mTorr and 5mTorr YSZ ,electrolyte at 500 °C.

The power density of the fuel cell increases with the increase of the current density. When the power density of the fuel cell reaches the peak value, it begins to decrease with the increase of the current density. In the fuel cell design, it is generally designed to work at the peak or low power density—some value. At current densities below the peak power density, voltage efficiency increases while power density decreases. Both voltage efficiency and power density decrease at current densities above the power density maximum. Generally speaking, the more current a fuel cell outputs, the greater the loss. This includes three significant fuel cell losses: activation loss caused by reaction kinetics, ohmic loss, ohmic losses due to ionic and electronic conduction, and concentration losses due to mass transport. The above three fuel cell losses determine the characteristic shape of the I-V curve of the fuel cell. The activation loss mainly affects the initial part of the I-V curve, the ohmic loss is mainly reflected in the middle part of the curve, and the concentration loss is most significant at the end of the curve.

When the sputtering pressure is 10mTorr and 20mTorr, the voltage shows a precarious state due to the generation of pores of different sizes in the electrolyte film. The graph of voltage change with time is shown in Figure 25. As the test time increases, the voltage of 10mTorr at 370s and 20mTorr at 467s drops sharply, indicating that the performance of the fuel cell has been affected, and the imbalance of the fuel cell itself is what we consider—unwanted things to happen.
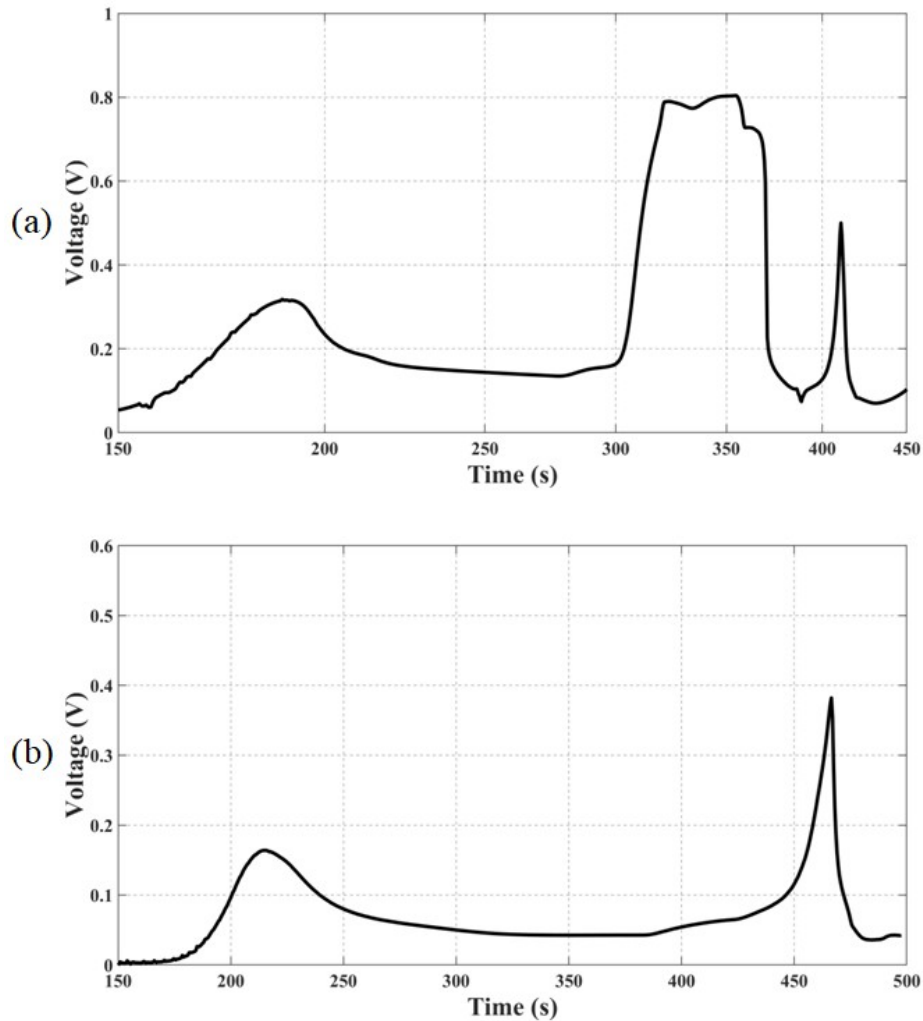
Figure 25. Voltage-time curves of AAO-based TF-SOFC at 500 °C for (a) 10mTorr and (b) 20mTorr YSZ electrolytes.

To gain a more detailed understanding of the electrochemical behavior of the fuel cell, EIS was performed with a bias voltage of 1 V, and the EIS spectra at 3mTorr and 5mTorr sputtering pressures are shown in Figure 26. However, because none of the EIS patterns in the figure intersect the X-axis, the ohmic loss and the polarization loss of the fuel cell electrode under different sputtering pressures cannot be obtained.

Because it uses EIS to regard an electrochemical system as an equivalent circuit, this equivalent circuit is composed of essential elements such as resistance (R), capacitance (C), and inductance (L) in

different ways, such as series or parallel combination and made it. Therefore, through EIS, the composition of the equivalent circuit and the size of each element can be determined. Furthermore, the electrochemical meaning of these elements can be used to analyze the structure of the electrochemical system and the properties of the electrode process. In the EIS measurement of the solid electrode, it is found that the curve always deviates from the semicircular trajectory more or less and appears as a circular arc, which is called the capacitive reactance arc. This phenomenon is called the "dispersion effect". The reason is generally related to the in homogeneity of the electrode surface, the adsorption layer on the electrode surface, and the poor conductivity of the solution, which reflects the deviation of the electrode electric double layer from the ideal capacitance.

Faraday process can be divided into two processes, the charge transfer process, and the material transfer process. When ω approaches 0, it is in the low-frequency region, which is controlled by material transfer; when ω is large, it is in the high-frequency region, dominated by charge transfer, and the period of change is too short for materials transfer to occur in time that is the effect of the Warburg impedance disappears. Usually, the high-frequency range is $10^3 \sim 10^4 \mathrm{Hz}$, while the low-frequency range is $10^{-3} \sim 10^3 \mathrm{Hz}$. It should be noted that for the same impedance spectrum, more than an A circuit can be fitted and analyzed, so relying on the equivalent circuit to infer the electrochemical reaction process is a highly subjective method.

In order to observe the electrochemical behavior more clearly and intuitively, ZView is used to fit the experimental data. The fitting gives the physical meaning of the components in the equivalent circuit to better explain the electrochemical impedance spectrum. The fitting results are shown in Figure 27. As shown, in the fitted circuit, R1 is the

ohmic impedance, R2 is the transfer resistance of the charge, CPE1 is the constant phase angle element, W1 is the Warburg impedance, a composite element composed in parallel, and its frequency response is expressed on the impedance complex plane for a semicircle.

It can be seen from the EIS result graph that in the high-frequency region, the ohmic impedance of the film produced under the sputtering pressure of 3mTorr is $0.06\Omega cm^2$, which is much smaller than the ohmic impedance ($0.083\Omega cm^2$) under 5mTorr. For the YSZ electrolyte film, ohmic impedance The resistance belongs to the ion conduction resistance, indicating that in practical applications, 3mTorr is more conducive to the conduction of ions; and in the low-frequency range, the charge transfer resistance of 3mTorr is $0.316\Omega cm^2$, which is also less than the charge transfer resistance of 5mTorr ($0.751\,\Omega cm^2$), indicating that under 3mTorr The prepared electrolyte films have faster charge transferability. In contrast, the diffusion impedance obtained by 3mTorr is smaller than that of 5mTorr, indicating that its diffusion speed is faster, which is more conducive to improving fuel cell performance.
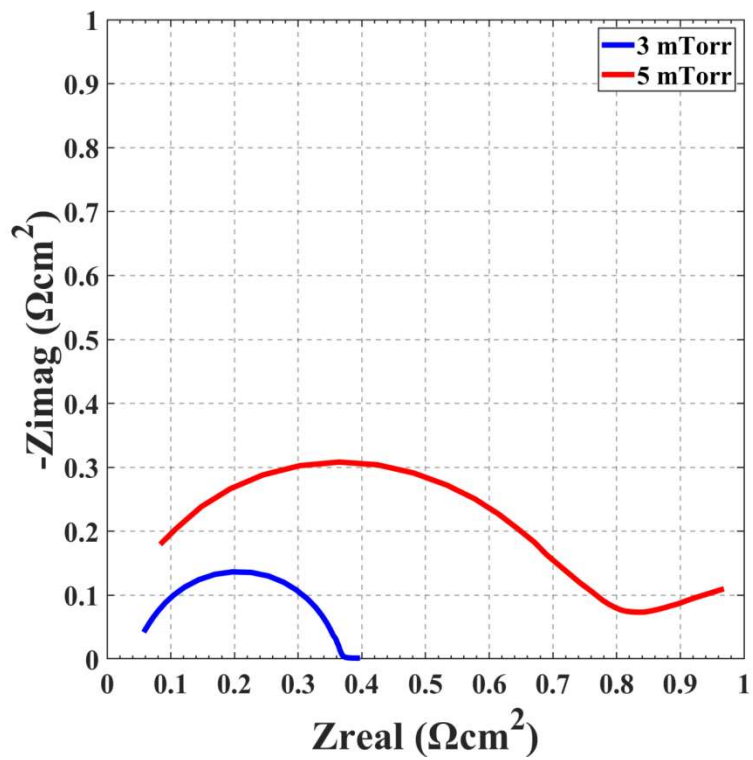
Figure 26. Electrochemical impedance spectroscopy (EIS) conducted at 1V.

Chi-Squared = 0.0018
Sum of Sqr = 0.1375

● Run Fitting / Selected Pts.

R1   CPE1   W1

R2

(b)

Element	Freedom	Value	Error	Error%
R1	Free(+)	5.2804E-7	0.29954	5.6727E07
CPE1-T	Free(+)	1.4651E-5	1.2889E-06	8.7974
CPE1-P	Free(+)	0.88439	0.013504	1.5269
R2	Free(+)	31.41	1.0406	3.313
W1-R	Free(+)	5.147	67.606	1313.5
W1-T	Free(+)	0.15402	43.904	28505
W1-P	Free(+)	0.029991	0.10793	359.87

Chi-Squared = 0.0002
Sum of Sqr = 0.0145

● Run Fitting / Selected Pts.

R1   CPE1   W1

R2

(c)

Element	Freedom	Value	Error	Error%
R1	Free(?)	-8.157	3.8947	47.747
CPE1-T	Free(+)	3.7275E-7	3.5197E-08	9.4425
CPE1-P	Free(+)	0.88847	0.010775	1.2128
R2	Free(+)	66.37	2.3558	3.5495
W1-R	Free(+)	109	46.536	42.694
W1-T	Free(+)	3.492	7.0016	200.5
W1-P	Free(+)	0.16606	0.039353	23.698

Figure 27. (a) Fitted circuit (b) 3mTorr fitting data (c) 5mTorr fitting data.

CHAPTER5. Summary and Future

The solid oxide fuel cell is the third-generation fuel cell system with the highest energy conversion efficiency. Moreover, the operating temperature of the fuel cell can be reduced by the method of electrolyte thin film formation to improve the operational performance of the fuel cell. In this paper, the fuel cell electrolyte film was prepared by magnetron sputtering technology in physical vapor deposition, and the influence of different sputtering parameters on the electrolyte film was studied. As well as performing stress studies on thin films using XRD techniques, thin-film stress studies aim to measure the magnitude and nature of various thin-film stresses.

RF magnetron sputtering of YSZ electrolyte films was carried out at different sputtering pressures of 3, 5, 10, and 20mTorr to find the optimal process conditions for YSZ to prepare AAO-based thin-film solid oxide fuel cells. According to the analysis of the experimental results, with the incr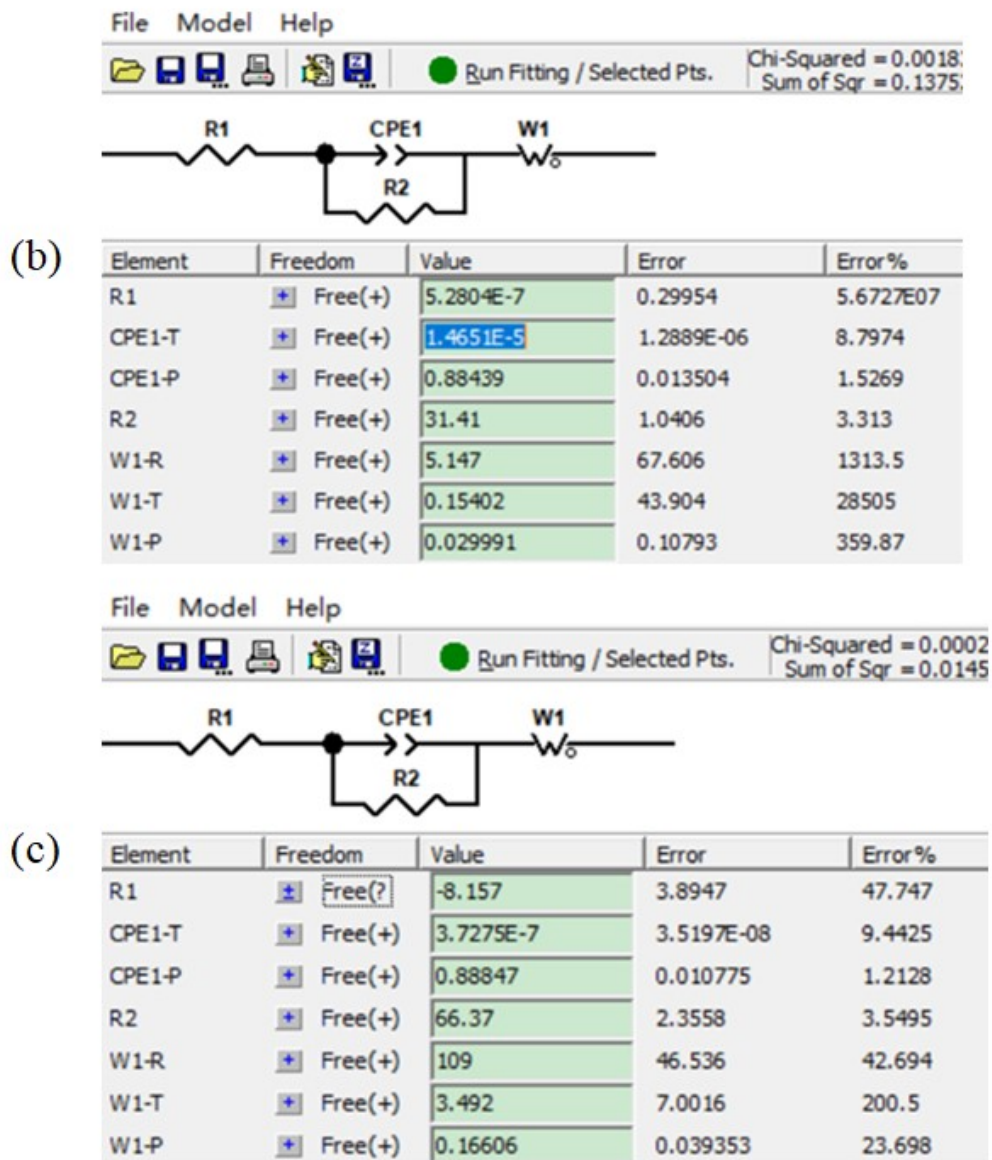ease of the sputtering pressure, the surface roughness of the YSZ film increases and the grains show a neat columnar arrangement. The stress state of the film changes from compressive stress to tensile stress with the increase of sputtering pressure. The existence of tensile stress promotes the vertical upward growth of crystal grains, resulting in the formation of pores of different sizes, which affects the film's performance. The thin film exhibited the densest film morphology under the sputtering pressure of 3mTorr, and the compressive stress promoted the growth of grains in the dense direction. At the same time, other factors such as sputtering power, the distance from the target to the substrate, and the substrate temperature will affect the nanostructure of the electrolyte film, so it is necessary to choose appropriate sputtering conditions.

Finally, electrochemical characterization of the films prepared under different sputtering pressures was carried out. The results showed that at 500°C, when the sputtering pressure was 3mTorr, a thin-film fuel cell with a 2.20 μm thick YSZ electrolyte was obtained to achieve an OCV of about 1.043 V and the maximum peak power density of 1.593W/cm^2. It is about 1.2 times higher than the peak power density (1.327 W/cm^2) of thin-film fuel cells fabricated at 5mTorr sputtering pressure. In summary, the electrolyte films prepared under the sputtering pressure of 3mTorr exhibited the best stress state and the densest electrolyte structure.
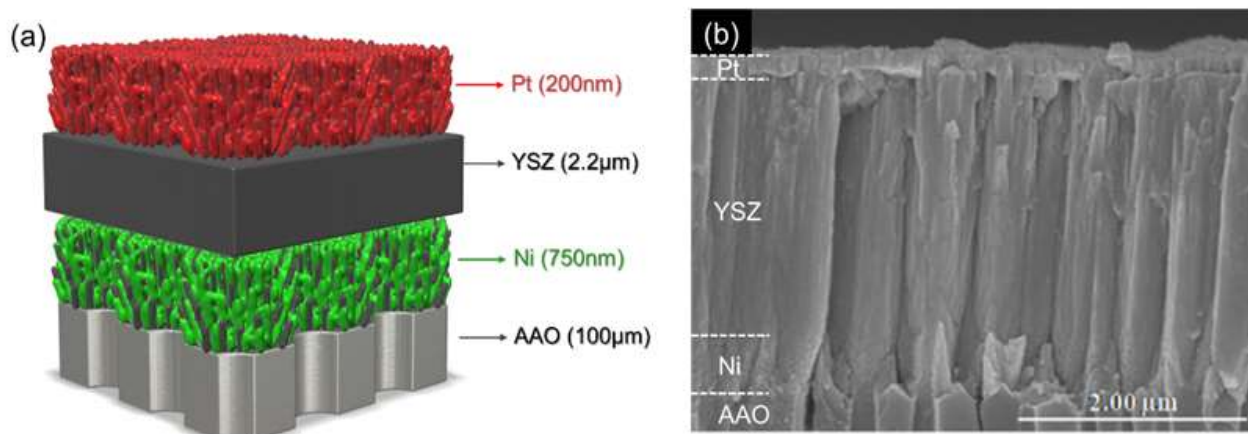
Figure 28. (a) Illustration of AAO-based thin film SOFC, (b) Cross-sectional FE-SEM images of YSZ electrolytes deposited on AAO substrates at 3mTorr.

Compared with the working temperature of a proton exchange membrane fuel cell at 80 °C, the working temperature of a solid oxide fuel cell can be as high as about 1000 °C, and the primary power generation efficiency can reach 60%, which is more suitable for large-scale power supply and integrated power generation. In addition to high power generation efficiency, solid oxide fuel cell power generation technology has high-quality waste heat. The temperature can

be as high as 600°C, so it can also be used for combined heat and power, and the efficiency can reach more than 90%. Therefore, it can be said that distributed power generation based on solid fuel cells is the most efficient and environmentally friendly gas power generation technology.

Figure 29 shows the maximum power densities achieved in previous studies and this work using AAO substrates and YSZ-based electrolytes. It is important to note that most other studies have used Pt as an electrode, which limits the operating temperatures to below 500°C due to the agglomeration of Pt at higher temperatures. This study developed a novel thin-film solid oxide fuel cell with excellent stability and high performance at 500℃. In addition, the maximum power objective of the fuel cell was increased by about four times[105]–[109].
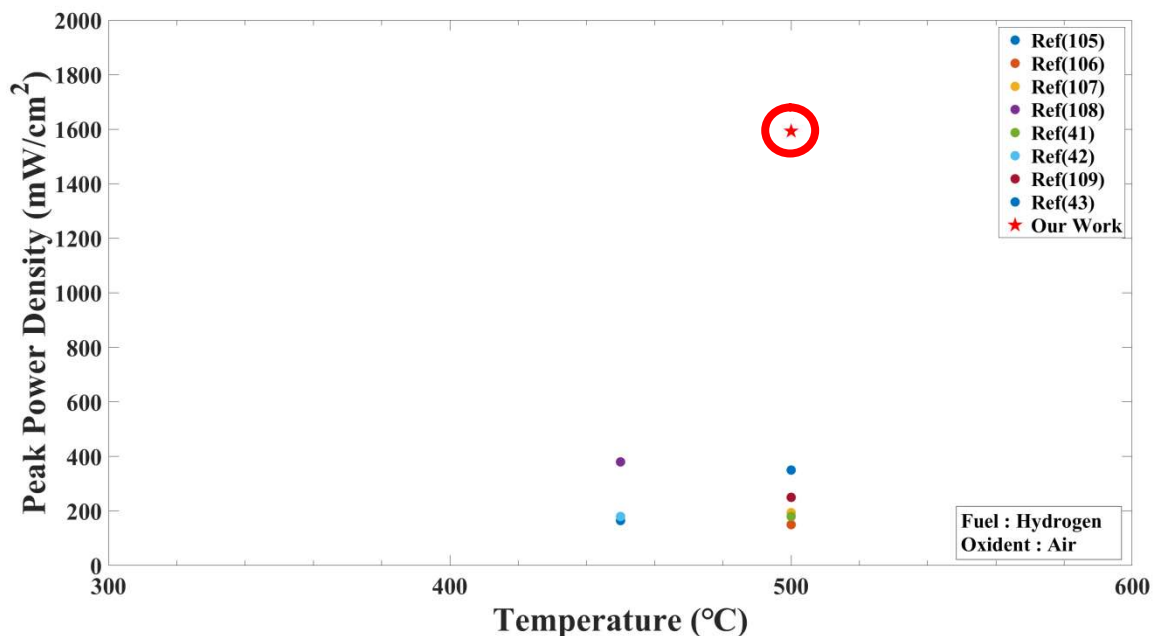
Figure 29. Performance comparison with other works using AAO substrate and YSZ electrolyte.

From Table 3, we can see that compared with the traditional YSZ electrolyte fuel cell, the YSZ electrolyte fuel cell fabricated by sputtering has a faster deposition rate and lower price.

Material	Thickness	Deposition Rate	Area	Process Unit Price
Conventional YSZ	1~3um	~ 24hour	10cm x 10cm	4~7$
YSZ by Sputter	1~3um	4nm/sec @600eV	10cm x 10cm	90cent

Table 3. YSZ electrolyte production cost analysis.

Regarding the cost of the sputtering process, the cost of maintenance, depreciation, utilities, and labor increases with time, and the cost of materials increases with the increase of film thickness.

Internationally, the application of SOFC has been relatively mature. However, because SOFC is a project that consumes enormous human resources and financial resources, few companies can genuinely realize large-scale commercial supply. Internationally renowned companies include Bloom Energy in the United States, Ceres Power in the United Kingdom, Elcogen in Estonia, Mitsubishi Heavy Industries and Kyocera in Japan, and KCERACELL, KOREA SOFC FORUM, and HNPOWER in Korea. However, in terms of annual power generation, no more than ten global SOFC companies can reach the megawatt level.

According to a report released by Markets and Markets, an international market research organization, the power generation sector accounted for the largest solid oxide fuel cell market share in 2021. The global solid oxide fuel cells market size was valued at USD 339.8 million in 2021 and is expected to expand at a compound annual growth rate of 40.7% from 2022 to 2030, as shown in Figures 30 and 31.

Solid oxide fuel cells have extensive application prospects. They use

solid ionic conductors as electrolytes, have a conversion efficiency of about 60%, can use a variety of fuels, and can be used in stationary power stations, household power sources, ship power, automotive power, space aerospace, and many other fields. In addition, corrosion and electrolyte loss caused by liquid electrolytes are avoided due to the use of an all-solid-state fuel cell structure. With further breakthroughs in solid oxide fuel cell technology, it is expected to be widely used in the future.
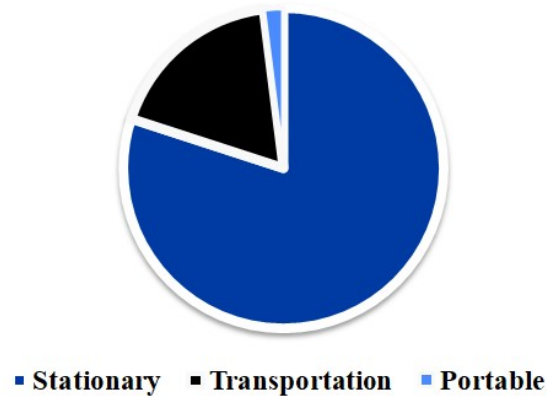
Figure 30. The proportion of global fuel cell shipments in different application fields in 2020.
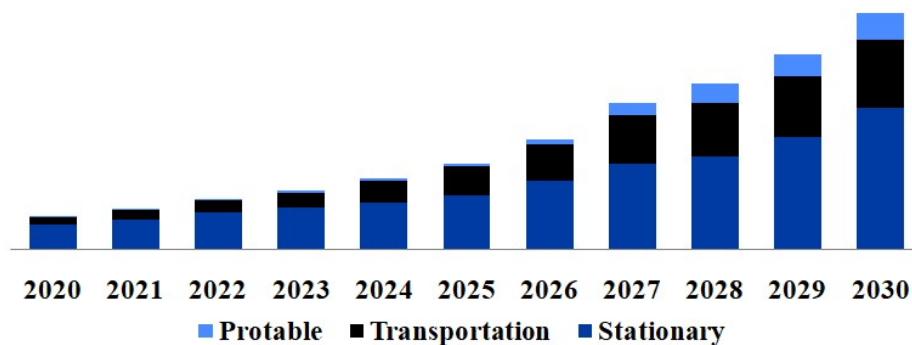
Figure 31. Trend chart of global fuel cell shipments in different application fields from 2020 to 2030.

REFERENCE

[1] K. Kordesch and J. Oliveira, 'Fuel cells: the present state of the technology and future applications, with special consideration of the alkaline hydrogen/oxygen (air) systems', *Int. J. Hydrog. Energy*, vol. 13, no. 7, pp. 411–427, 1988, doi: 10.1016/0360-3199(88)90127-9.

[2] D. Daggett, S. Eelman, and G. Kristiansson, 'Fuel Cell APU', presented at the AIAA International Air and Space Symposium and Exposition: The Next 100 Years, Dayton, Ohio, Jul. 2003. doi: 10.2514/6.2003-2660.

[3] F. T. Bacon, 'Fuel cells, past, present and future', *Electrochimica Acta*, vol. 14, no. 7, pp. 569–585, 1969.

[4] L. Mond and C. Langer, 'V. A new form of gas battery', *Proc. R. Soc. Lond.*, vol. 46, no. 280–285, pp. 296–304, 1890.

[5] P. T. Maxwell and R. N. Parker, 'The Apollo Auxiliary Power Supply System, Project Apollo', 1962.

[6] N. P. Brandon and D. J. Brett, 'Engineering porous materials for fuel cell applications', *Philos. Trans. R. Soc. Math. Phys. Eng. Sci.*, vol. 364, no. 1838, pp. 147–159, 2006.

[7] U. Lucia, 'Overview on fuel cells', *Renew. Sustain. Energy Rev.*, vol. 30, pp. 164–169, Feb. 2014, doi: 10.1016/j.rser.2013.09.025.

[8] G. F. McLean, T. Niet, S. Prince-Richard, and N. Djilali, 'An assessment of alkaline fuel cell technology', *Int. J. Hydrog. Energy*,

vol. 27, no. 5, pp. 507–526, 2002.

[9] N. Sammes, R. Bove, and K. Stahl, 'Phosphoric acid fuel cells: Fundamentals and applications', *Curr. Opin. Solid State Mater. Sci.*, vol. 8, no. 5, pp. 372–378, 2004.

[10] N. Q. Minh, 'Solid oxide fuel cell technology—features and applications', *Solid State Ion.*, vol. 174, no. 1–4, pp. 271–277, 2004.

[11] R. M. Ormerod, 'Solid oxide fuel cells', *Chem. Soc. Rev.*, vol. 32, no. 1, pp. 17–28, Dec. 2003, doi: 10.1039/b105764m.

[12] S. Singhal, 'Advances in solid oxide fuel cell technology', *Solid State Ion.*, vol. 135, no. 1–4, pp. 305–313, Nov. 2000, doi: 10.1016/S0167-2738(00)00452-5.

[13] A. B. Stambouli and E. Traversa, 'Solid oxide fuel cells (SOFCs): a review of an environmentally clean and efficient source of energy', *Renew. Sustain. Energy Rev.*, vol. 6, no. 5, pp. 433–455, Oct. 2002, doi: 10.1016/S1364-0321(02)00014-X.

[14] A. Choudhury, H. Chandra, and A. Arora, 'Application of solid oxide fuel cell technology for power generation—A review', *Renew. Sustain. Energy Rev.*, vol. 20, pp. 430–442, Apr. 2013, doi: 10.1016/j.rser.2012.11.031.

[15] F. Barbir, 'EFF.tCIENCY AND ECONOMICS OF PROTON EXCHANGE MEMBRANE (PEM) FUEL CELLS', p. 11.

[16] G. Cacciola, 'Technology up date and new strategies on fuel cells',

J. Power Sources, vol. 100, no. 1–2, pp. 67–79, Nov. 2001, doi: 10.1016/S0378-7753(01)00884-9.

[17] P. Costamagna and S. Srinivasan, 'Quantum jumps in the PEMFC science and technology from the 1960s to the year 2000 Part II. Engineering, technology development and application aspects$', *J. Power Sources*, p. 17, 2001.

[18] V. Mehta and J. S. Cooper, 'Review and analysis of PEM fuel cell design and manufacturing', *J. Power Sources*, p. 22, 2003.

[19] J.-H. Wee, 'Applications of proton exchange membrane fuel cell systems', *Renew. Sustain. Energy Rev.*, vol. 11, no. 8, pp. 1720–1738, Oct. 2007, doi: 10.1016/j.rser.2006.01.005.

[20] S. Gamburzev and A. J. Appleby, 'Recent progress in performance improvement of the proton exchange membrane fuel cell (PEMFC)', *J. Power Sources*, vol. 107, no. 1, pp. 5–12, Apr. 2002, doi: 10.1016/S0378-7753(01)00970-3.

[21] N. Mahato, A. Banerjee, A. Gupta, S. Omar, and K. Balani, 'Progress in material selection for solid oxide fuel cell technology: A review', *Prog. Mater. Sci.*, vol. 72, pp. 141–337, Jul. 2015, doi: 10.1016/j.pmatsci.2015.01.001.

[22] D. S. McLachlan, M. Blaszkiewicz, and R. E. Newnham, 'Electrical Resistivity of Composites', *J. Am. Ceram. Soc.*, vol. 73, no. 8, pp. 2187–2203, Aug. 1990, doi:

10.1111/j.1151-2916.1990.tb07576.x.

[23] O. Yamamoto, 'Solid oxide fuel cells: fundamental aspects and prospects', *Electrochimica Acta*, vol. 45, no. 15–16, pp. 2423–2435, May 2000, doi: 10.1016/S0013-4686(00)00330-3.

[24] G. N. Parsons, S. M. George, and M. Knez, 'Progress and future directions for atomic layer deposition and ALD-based chemistry', *MRS Bull.*, vol. 36, no. 11, pp. 865–871, Nov. 2011, doi: 10.1557/mrs.2011.238.

[25] K.-W. Chour, J. Chen, and R. Xu, 'Metal-organic vapor deposition of YSZ electrolyte layers for solid oxide fuel cell applications', *Thin Solid Films*, vol. 304, no. 1–2, pp. 106–112, Jul. 1997, doi: 10.1016/S0040-6090(97)00017-5.

[26] E.-O. Oh *et al.*, 'Thin film yttria-stabilized zirconia electrolyte for intermediate-temperature solid oxide fuel cells (IT-SOFCs) by chemical solution deposition', *J. Eur. Ceram. Soc.*, vol. 32, no. 8, pp. 1733–1741, Jul. 2012, doi: 10.1016/j.jeurceramsoc.2012.01.021.

[27] H. Sasaki, S. Otoshi, M. Suzuki, T. Sogi, A. Kajimura, and M. Ippommatsu, 'Fabrication of high power density tubular type solid oxide fuel cells', p. 4.

[28] S. Ji *et al.*, 'Fabrication of low-temperature solid oxide fuel cells with a nanothin protective layer by atomic layer deposition', *Nanoscale Res. Lett.*, vol. 8, no. 1, p. 48, Dec. 2013, doi:

10.1186/1556-276X-8-48.

[29] A. Baptista, F. J. G. Silva, J. Porteiro, J. L. Míguez, G. Pinto, and L. Fernandes, 'On the Physical Vapour Deposition (PVD): Evolution of Magnetron Sputtering Processes for Industrial Applications', *Procedia Manuf.*, vol. 17, pp. 746–757, 2018, doi: 10.1016/j.promfg.2018.10.125.

[30] P. Srivastava *et al.*, 'Electrode supported solid oxide fuel cells: Electrolyte films prepared by DC magnetron sputtering', *Solid State Ion.*, vol. 99, no. 3–4, pp. 311–319, Aug. 1997, doi: 10.1016/S0167-2738(97)00248-8.

[31] H. Wang *et al.*, 'Preparation of YSZ films by magnetron sputtering for anode-supported SOFC', *Solid State Ion.*, vol. 192, no. 1, pp. 413–418, Jun. 2011, doi: 10.1016/j.ssi.2010.05.022.

[32] H. Sun, W. Ma, J. Yu, X. Chen, W. Sen, and Y. Zhou, 'Preparation and characterization of La0.9Sr0.1Ga0.8Mg0.2O3−δ thin film electrolyte deposited by RF magnetron sputtering on the porous anode support for IT-SOFC', *Vacuum*, vol. 86, no. 8, pp. 1203–1209, Feb. 2012, doi: 10.1016/j.vacuum.2011.11.002.

[33] S. P. S. Shaikh, A. Muchtar, and M. R. Somalu, 'A review on the selection of anode materials for solid-oxide fuel cells', *Renew. Sustain. Energy Rev.*, vol. 51, pp. 1–8, Nov. 2015, doi: 10.1016/j.rser.2015.05.069.

[34] S. de Souza, 'Thin-film solid oxide fuel cell with high performance at low-temperature', *Solid State Ion.*, vol. 98, no. 1–2, pp. 57–61, Jun. 1997, doi: 10.1016/S0167-2738(96)00525-5.

[35] Yang, Seon-Ho and Choi, Hyung-Wook, 'Fabrication of YSZ/GDC Bilayer Electrolyte Thin Film for Solid Oxide Fuel Cells', *Trans. Electr. Electron. Mater.*, vol. 15, no. 4, pp. 189–192, 2014, doi: 10.4313/TEEM.2014.15.4.189.

[36] S. Cho, Y. Kim, J.-H. Kim, A. Manthiram, and H. Wang, 'High power density thin film SOFCs with YSZ/GDC bilayer electrolyte', *Electrochimica Acta*, vol. 56, no. 16, pp. 5472–5477, Jun. 2011, doi: 10.1016/j.electacta.2011.03.039.

[37] J. Yan, H. Matsumoto, M. Enoki, and T. Ishihara, 'High-Power SOFC Using La[sub 0.9]Sr[sub 0.1]Ga[sub 0.8]Mg[sub 0.2]O[sub 3−δ]/Ce[sub 0.8]Sm[sub 0.2]O[sub 2−δ] Composite Film', *Electrochem. Solid-State Lett.*, vol. 8, no. 8, p. A389, 2005, doi: 10.1149/1.1943568.

[38] J. S. Ahn, S. Omar, H. Yoon, J. C. Nino, and E. D. Wachsman, 'Performance of anode-supported solid oxide fuel cell using novel ceria electrolyte', *J. Power Sources*, vol. 195, no. 8, pp. 2131–2135, Apr. 2010, doi: 10.1016/j.jpowsour.2009.09.009.

[39] H. Huang, M. Nakamura, P. Su, R. Fasching, Y. Saito, and F. B. Prinz, 'High-Performance Ultrathin Solid Oxide Fuel Cells for

Low-Temperature Operation', *J. Electrochem. Soc.*, vol. 154, no. 1, p. B20, 2007, doi: 10.1149/1.2372592.

[40]C.-W. Kwon, J.-I. Lee, K.-B. Kim, H.-W. Lee, J.-H. Lee, and J.-W. Son, 'The thermomechanical stability of micro-solid oxide fuel cells fabricated on anodized aluminum oxide membranes', *J. Power Sources*, vol. 210, pp. 178–183, Jul. 2012, doi: 10.1016/j.jpowsour.2012.03.020.

[41] S. Ji, G. Y. Cho, W. Yu, P.-C. Su, M. H. Lee, and S. W. Cha, 'Plasma-Enhanced Atomic Layer Deposition of Nanoscale Yttria-Stabilized Zirconia Electrolyte for Solid Oxide Fuel Cells with Porous Substrate', *ACS Appl. Mater. Interfaces*, vol. 7, no. 5, pp. 2998–3002, Feb. 2015, doi: 10.1021/am508710s.

[42] S. Ha, P.-C. Su, and S.-W. Cha, 'Combinatorial deposition of a dense nano-thin film YSZ electrolyte for low temperature solid oxide fuel cells', *J. Mater. Chem. A*, vol. 1, no. 34, p. 9645, 2013, doi: 10.1039/c3ta11758h.

[43] C.-W. Kwon, J.-W. Son, J.-H. Lee, H.-M. Kim, H.-W. Lee, and K.-B. Kim, 'High-Performance Micro-Solid Oxide Fuel Cells Fabricated on Nanoporous Anodic Aluminum Oxide Templates', *Adv. Funct. Mater.*, vol. 21, no. 6, pp. 1154–1159, Mar. 2011, doi: 10.1002/adfm.201002137.

[44] S. Hong, S. Oh, H. J. Kim, Y. Lim, J. An, and Y.-B. Kim,

'Enhanced Thermal Stability of a Gadolinia-Doped Ceria Capped Metal Electrode for Durable Low-Temperature Solid Oxide Fuel Cells', *J. Electrochem. Soc.*, vol. 164, no. 13, pp. F1301–F1306, 2017, doi: 10.1149/2.0261713jes.

[45] Y. Lee *et al.*, 'Nickel-based bilayer thin-film anodes for low-temperature solid oxide fuel cells', *Energy*, vol. 161, pp. 1133–1138, Oct. 2018, doi: 10.1016/j.energy.2018.07.147.

[46] M. S. Lee *et al.*, 'Nanoporous nickel thin film anode optimization for low-temperature solid oxide fuel cells', *Int. J. Hydrog. Energy*, vol. 46, no. 73, pp. 36445–36453, Oct. 2021, doi: 10.1016/j.ijhydene.2021.08.138.

[47] Y. Li, J. Chen, P. Cai, and Z. Wen, 'An electrochemically neutralized energy-assisted low-cost acid-alkaline electrolyzer for energy-saving electrolysis hydrogen generation', *J. Mater. Chem. A*, vol. 6, no. 12, pp. 4948–4954, 2018, doi: 10.1039/C7TA10374C.

[48] S. Swann, 'Magnetron sputtering', *Phys. Technol.*, vol. 19, no. 2, pp. 67–75, Mar. 1988, doi: 10.1088/0305-4624/19/2/304.

[49] A. Baptista, F. Silva, J. Porteiro, J. Míguez, and G. Pinto, 'Sputtering Physical Vapour Deposition (PVD) Coatings: A Critical Review on Process Improvement and Market Trend Demands', *Coatings*, vol. 8, no. 11, p. 402, Nov. 2018, doi: 10.3390/coatings8110402.

[50] Q. Xiao, H. He, S. Shao, J. Shao, and Z. Fan, 'Influences of deposition rate and oxygen partial pressure on residual stress and microstructure of YSZ thin films', *Thin Solid Films*, vol. 517, no. 15, pp. 4295–4298, Jun. 2009, doi: 10.1016/j.tsf.2008.11.138.

[51] M. Liu *et al.*, 'Influence of radio frequency magnetron sputtering parameters on the structure and performance of SiC films', *Ceram. Int.*, vol. 47, no. 17, pp. 24098–24105, Sep. 2021, doi: 10.1016/j.ceramint.2021.05.120.

[52] A. Sengupta and C. K. Sarkar, *Introduction to nano: basics to nanoscience and nanotechnology*. Springer, 2015.

[53] J. L. Vossen, W. Kern, and W. Kern, *Thin film processes II*, vol. 2. Gulf Professional Publishing, 1991.

[54] A. M. Chaparro, A. J. Martín, M. A. Folgado, B. Gallardo, and L. Daza, 'Comparative analysis of the electroactive area of Pt/C PEMFC electrodes in liquid and solid polymer contact by underpotential hydrogen adsorption/desorption', *Int. J. Hydrog. Energy*, vol. 34, no. 11, pp. 4838–4846, Jun. 2009, doi: 10.1016/j.ijhydene.2009.03.053.

[55] A. O. Adeyeye and G. Shimon, 'Growth and Characterization of Magnetic Thin Film and Nanostructures', in *Handbook of Surface Science*, vol. 5, Elsevier, 2015, pp. 1–41. doi: 10.1016/B978-0-444-62634-9.00001-1.

[56] N. Kaiser, 'Review of the fundamentals of thin-film growth', *Appl. Opt.*, vol. 41, no. 16, p. 3053, Jun. 2002, doi: 10.1364/AO.41.003053.

[57] A. Matsuda, 'Thin-Film Silicon –Growth Process and Solar Cell Application–', *Jpn. J. Appl. Phys.*, vol. 43, no. 12, pp. 7909–7920, Dec. 2004, doi: 10.1143/JJAP.43.7909.

[58] S. Kang, P. Heo, Y. H. Lee, J. Ha, I. Chang, and S.-W. Cha, 'Low intermediate temperature ceramic fuel cell with Y-doped BaZrO3 electrolyte and thin film Pd anode on porous substrate', *Electrochem. Commun.*, vol. 13, no. 4, pp. 374–377, Apr. 2011, doi: 10.1016/j.elecom.2011.01.029.

[59] Z. Yao, C. Wang, Y. Li, and N.-Y. Kim, 'AAO-assisted synthesis of highly ordered, large-scale TiO2 nanowire arrays via sputtering and atomic layer deposition', *Nanoscale Res. Lett.*, vol. 10, no. 1, p. 166, Dec. 2015, doi: 10.1186/s11671-015-0872-9.

[60] S. Liu, Z. Xiong, C. Zhu, M. Li, M. Zheng, and W. Shen, 'Fast anodization fabrication of AAO and barrier perforation process on ITO glass', *Nanoscale Res. Lett.*, vol. 9, no. 1, p. 159, Dec. 2014, doi: 10.1186/1556-276X-9-159.

[61] Z. Zhou *et al.*, 'Novel synthesis of highly active Pt/C cathode electrocatalyst for direct methanol fuel cell', *Chem. Commun.*, no. 3, pp. 394–395, Jan. 2003, doi: 10.1039/b211075j.

[62] R. Othman, A. L. Dicks, and Z. Zhu, 'Non precious metal catalysts for the PEM fuel cell cathode', *Int. J. Hydrog. Energy*, vol. 37, no. 1, pp. 357–372, Jan. 2012, doi: 10.1016/j.ijhydene.2011.08.095.

[63] N. Pryds, K. Rodrigo, S. Linderoth, and J. Schou, 'On the growth of gadolinia-doped ceria by pulsed laser deposition', *Appl. Surf. Sci.*, vol. 255, no. 10, pp. 5232–5235, Mar. 2009, doi: 10.1016/j.apsusc.2008.07.134.

[64] X.T.Xiong，L.C.Yan, 'Technology and Properties of Chromium Oxide Thin Films Prepared by Radio Frequency Reactive Magnetron Sputtering', *J. Univ. Sci. Technol. Beijing*, vol. Vol.27, no. No.2, Apr. 2005.

[65] P.Gao,X.Jun,Y.Piao, 'Influence of Sputtering Power on Microstructure of Carbon Nitride Flims', *J. Vac. Sci. Technol.*, vol. Vol.25, no. No.5, p. 350.

[66] Y. Yamamura and H. Tawara, 'ENERGY DEPENDENCE OF ION-INDUCED SPUTTERING YIELDS FROM MONATOMIC SOLIDS AT NORMAL INCIDENCE', *At. Data Nucl. Data Tables*, vol. 62, no. 2, pp. 149–253, Mar. 1996, doi: 10.1006/adnd.1996.0005.

[67] S. D. Ekpe, L. W. Bezuidenhout, and S. K. Dew, 'Deposition rate model of magnetron sputtered particles', *Thin Solid Films*, vol. 474,

no. 1–2, pp. 330–336, Mar. 2005, doi: 10.1016/j.tsf.2004.09.007.

[68] C. Su-yu and C. Kai-jia, 'Computation on heat of formation and EOS of alloy by a refined TFD model', *Acta Phys. Sin. Overseas Ed.*, vol. 2, no. 6, pp. 439–448, Jun. 1993, doi: 10.1088/1004-423X/2/6/005.

[69] C. Su-yu and C. Kai-jia, 'Analysis and computation of the internal stress in thin films', *Inst. Nucl. Technol.*, no. 710024.

[70] H. Windischmann, 'Intrinsic stress in sputtered thin films', p. 7.

[71] E. Chason, B. W. Sheldon, L. B. Freund, J. A. Floro, and S. J. Hearne, 'Origin of Compressive Residual Stress in Polycrystalline Thin Films', *Phys. Rev. Lett.*, vol. 88, no. 15, p. 156103, Mar. 2002, doi: 10.1103/PhysRevLett.88.156103.

[72] G. C. A. M. Janssen, 'Stress and strain in polycrystalline thin films', *Thin Solid Films*, vol. 515, no. 17, pp. 6654–6664, Jun. 2007, doi: 10.1016/j.tsf.2007.03.007.

[73] N. A. Mara and I. J. Beyerlein, 'Review: effect of bimetal interface structure on the mechanical behavior of Cu–Nb fcc–bcc nanolayered composites', *J. Mater. Sci.*, vol. 49, no. 19, pp. 6497–6516, Oct. 2014, doi: 10.1007/s10853-014-8342-9.

[74] G. W. Greenwood, 'Generation of internal stress and its effects', *Mater. Sci. Technol.*, vol. 26, no. 4, pp. 398–403, Apr. 2010, doi: 10.1179/026708309X12506933872946.

[75] H.P.Murbach and H.Wilman, 'The Origin of Stress in Metal Layers Condensed from the Vapour in High Vaccum', *Phys. Chem. Lab.*, 1953.

[76] D. W. Hoffman and J. A. Thornton, 'Compressive stress and inert gas in Mo films sputtered from a cylindrical-post magnetron with Ne, Ar, Kr, and Xe', *J. Vac. Sci. Technol.*, vol. 17, no. 1, pp. 380–383, Jan. 1980, doi: 10.1116/1.570394.

[77] D. W. Hoffman and C. M. Kukla, 'Determination of film stresses during sputter deposition using an *i n s i t u* probe', *J. Vac. Sci. Technol. Vac. Surf. Films*, vol. 3, no. 6, pp. 2600–2604, Nov. 1985, doi: 10.1116/1.572842.

[78] D. Rafaja, V. Valvoda, A. J. Perry, and J. R. Treglio, 'Depth profile of residual stress in metal-ion implanted TiN coatings', *Surf. Coat. Technol.*, vol. 92, no. 1–2, pp. 135–141, Jun. 1997, doi: 10.1016/S0257-8972(97)00013-3.

[79] Y. Oka, M. Kirinuki, Y. Nishimura, K. Azuma, E. Fujiwara, and M. Yatsuzuka, 'Measurement of residual stress in DLC films prepared by plasma-based ion implantation and deposition', *Surf. Coat. Technol.*, vol. 186, no. 1–2, pp. 141–145, Aug. 2004, doi: 10.1016/j.surfcoat.2004.04.010.

[80] M. Qasmi, P. Delobelle, F. Richard, and A. Bosseboeuf, 'Effect of the residual stress on the determination through nanoindentation

technique of the Young's modulus of W thin film deposit on SiO2/Si substrate', *Surf. Coat. Technol.*, vol. 200, no. 14–15, pp. 4185–4194, Apr. 2006, doi: 10.1016/j.surfcoat.2004.12.020.

[81] C. S. Litteken, S. Strohband, and R. H. Dauskardt, 'Residual stress effects on plastic deformation and interfacial fracture in thin-film structures', *Acta Mater.*, vol. 53, no. 7, pp. 1955–1961, Apr. 2005, doi: 10.1016/j.actamat.2005.01.005.

[82] W. L. Li, W. D. Fei, and T. Hanabusa, 'Effect of deposition condition on residual stress of iron nitride thin films prepared by magnetron sputtering and ion implantation', *Appl. Surf. Sci.*, vol. 252, no. 8, pp. 2847–2852, Feb. 2006, doi: 10.1016/j.apsusc.2005.04.043.

[83] J. Dean, T. Gu, and T. W. Clyne, 'Evaluation of residual stress levels in plasma electrolytic oxidation coatings using a curvature method', *Surf. Coat. Technol.*, vol. 269, pp. 47–53, May 2015, doi: 10.1016/j.surfcoat.2014.11.006.

[84] L. Pintschovius, V. Jung, E. Macherauch, and O. Vohringer, 'Residual Stress Measurements by means of Neutron Diffraction', p. 8.

[85] V. Pisarev, I. Odintsev, S. Eleonsky, and A. Apalkov, 'Residual stress determination by optical interferometric measurements of hole diameter increments', *Opt. Lasers Eng.*, vol. 110, pp. 437–456,

Nov. 2018, doi: 10.1016/j.optlaseng.2018.06.022.

[86] I. D. Wolf, 'Micro-Raman spectroscopy to study local mechanical stress in silicon integrated circuits', *Semicond. Sci. Technol.*, vol. 11, no. 2, pp. 139–154, Feb. 1996, doi: 10.1088/0268-1242/11/2/001.

[87] G. C. A. M. Janssen, M. M. Abdalla, F. van Keulen, B. R. Pujada, and B. van Venrooy, 'Celebrating the 100th anniversary of the Stoney equation for film stress: Developments from polycrystalline steel strips to single crystal silicon wafers', *Thin Solid Films*, vol. 517, no. 6, pp. 1858–1867, Jan. 2009, doi: 10.1016/j.tsf.2008.07.014.

[88] X. Feng, Y. Huang, and A. J. Rosakis, 'On the Stoney Formula for a Thin Film/Substrate System With Nonuniform Substrate Thickness', *J. Appl. Mech.*, vol. 74, no. 6, pp. 1276–1281, Nov. 2007, doi: 10.1115/1.2745392.

[89] E. Bemporad *et al.*, 'A critical comparison between XRD and FIB residual stress measurement techniques in thin films', *Thin Solid Films*, vol. 572, pp. 224–231, Dec. 2014, doi: 10.1016/j.tsf.2014.09.053.

[90] C.-H. Ma, J.-H. Huang, and H. Chen, 'Residual stress measurement in textured thin film by grazing-incidence X-ray diffraction', *Thin Solid Films*, vol. 418, no. 2, pp. 73–78, Oct. 2002, doi: 10.1016/S0040-6090(02)00680-6.

[91] E. Macherauch, 'X-ray stress analysis: Paper covers some rather important developments during the last decade, including new experimental results and theoretical aspects of X-ray stress analysis', *Exp. Mech.*, vol. 6, no. 3, pp. 140–153, Mar. 1966, doi: 10.1007/BF02326143.

[92] I. G. McDonald, W. M. Moehlenkamp, D. Arola, and J. Wang, 'Residual Stresses in Cu/Ni Multilayer Thin Films Measured Using the Sin2ψ Method', *Exp. Mech.*, vol. 59, no. 1, pp. 111–120, Jan. 2019, doi: 10.1007/s11340-018-00447-2.

[93] D. Quinn, S. Mark Spearing, and B. L. Wardle, 'Residual stress and microstructural evolution in thin film materials for a micro solid oxide fuel cell (SOFC).', *MRS Proc.*, vol. 854, p. U8.19, 2004, doi: 10.1557/PROC-854-U8.19.

[94] D. W. Hoffman, 'Perspective on stresses in magnetron-sputtered thin films', *J. Vac. Sci. Technol. Vac. Surf. Films*, vol. 12, no. 4, pp. 953–961, Jul. 1994, doi: 10.1116/1.579073.

[95] T. J. Vink, W. Walrave, J. L. C. Daams, A. G. Dirks, M. A. J. Somers, and K. J. A. van den Aker, 'Stress, strain, and microstructure in thin tungsten films deposited by dc magnetron sputtering', *J. Appl. Phys.*, vol. 74, no. 2, pp. 988–995, Jul. 1993, doi: 10.1063/1.354842.

[96] L. R. B. Elton and D. F. Jackson, 'X-Ray Diffraction and the

Bragg Law', *Am. J. Phys.*, vol. 34, no. 11, pp. 1036–1038, Nov. 1966, doi: 10.1119/1.1972439.

[97] G.E.M.Jauncey, 'The Scattering of X-rays and Bragg's Law', *Proc. Natl. Acad. Sci.*, vol. Volume 10, no. Number 2, Feb. 1924.

[98] P. Middha, O. R. Hansen, and I. E. Storvik, 'Validation of CFD-model for hydrogen dispersion', *J. Loss Prev. Process Ind.*, vol. 22, no. 6, pp. 1034–1038, Nov. 2009, doi: 10.1016/j.jlp.2009.07.020.

[99] Y. Sato, H. Iwabuchi, M. Groethe, E. Merilo, and S. Chiba, 'Experiments on hydrogen deflagration', *J. Power Sources*, vol. 159, no. 1, pp. 144–148, Sep. 2006, doi: 10.1016/j.jpowsour.2006.04.062.

[100] G. Chiodelli and L. Malavasi, 'Electrochemical open circuit voltage (OCV) characterization of SOFC materials', *Ionics*, vol. 19, no. 8, pp. 1135–1144, Aug. 2013, doi: 10.1007/s11581-013-0843-z.

[101] T. Miyashita, 'Empirical equation about open circuit voltage in SOFC', *J. Mater. Sci.*, vol. 40, no. 22, pp. 6027–6027, Nov. 2005, doi: 10.1007/s10853-005-4560-5.

[102] J. Joo and G. Choi, 'Open-circuit voltage of ceria-based thin film SOFC supported on nano-porous alumina', *Solid State Ion.*, vol. 178, no. 29–30, pp. 1602–1607, Dec. 2007, doi: 10.1016/j.ssi.2007.10.006.

[103] T. Matsui, T. Kosaka, M. Inaba, A. Mineshige, and Z. Ogumi, 'Effects of mixed conduction on the open-circuit voltage of intermediate-temperature SOFCs based on Sm-doped ceria electrolytes', *Solid State Ion.*, vol. 176, no. 7–8, pp. 663–668, Feb. 2005, doi: 10.1016/j.ssi.2004.10.010.

[104] T. Kawada, 'IONIC CONDUCI1VITY OF MONIWXOKILLON1TE/ALIC~LI SKLT MIXTURES', p. 4.

[105] J. Park, Y. Lee, I. Chang, W. Lee, and S. W. Cha, 'Engineering of the electrode structure of thin film solid oxide fuel cells', *Thin Solid Films*, vol. 584, pp. 125–129, Jun. 2015, doi: 10.1016/j.tsf.2014.11.018.

[106] S. Lee *et al.*, 'A nanoporous substrate-based low temperature solid oxide fuel cell using a thin film Ni anode', *Thin Solid Films*, vol. 666, pp. 177–181, Nov. 2018, doi: 10.1016/j.tsf.2018.09.039.

[107] T. Park *et al.*, 'Effect of anode morphology on the performance of thin film solid oxide fuel cell with PEALD YSZ electrolyte', *Int. J. Hydrog. Energy*, vol. 41, no. 22, pp. 9638–9643, Jun. 2016, doi: 10.1016/j.ijhydene.2016.04.092.

[108] S. Hong, J. Bae, B. Koo, and Y.-B. Kim, 'High-performance ultra-thin film solid oxide fuel cell using anodized-aluminum-oxide supporting structure', *Electrochem. Commun.*, vol. 47, pp. 1–4, Oct. 2014, doi: 10.1016/j.elecom.2014.07.008.

[109] I. Chang, S. Ji, J. Park, M. H. Lee, and S. W. Cha, 'Ultrathin YSZ Coating on Pt Cathode for High Thermal Stability and Enhanced Oxygen Reduction Reaction Activity', *Adv. Energy Mater.*, vol. 5, no. 10, p. 1402251, May 2015, doi: 10.1002/aenm.201402251.